contain substantial levels of σ, in excellent accord with experimental observation. Keefe *et al.* (1992) further determined TTT diagrams for both U720 and U720LI, which are shown in Figure 10.47. Decreasing the Cr levels must decrease the σ-solvus and, as the high-temperature part of the TTT diagram asymptotes to the σ-solvus temperature, the two TTT diagrams should have distinct and separate curves. Taking the σ-solvus calculated for U720 and U720LI, it was proposed (Saunders 1995, 1996c) that the TTT diagrams should have the form as shown in Fig. 10.48.

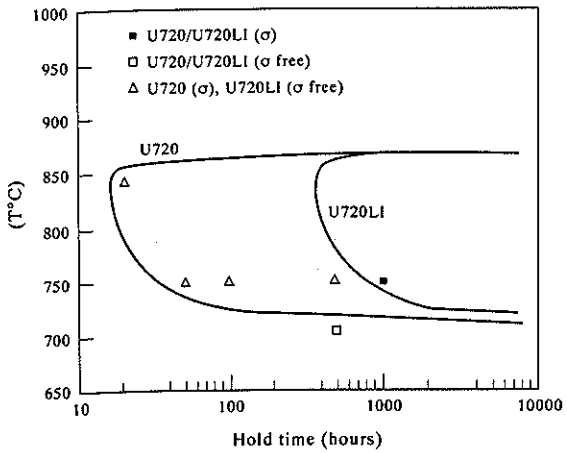

Figure 10.47 TTT diagrams for σ formation for U720 and U720LI after Keefe *et al.* (1992).

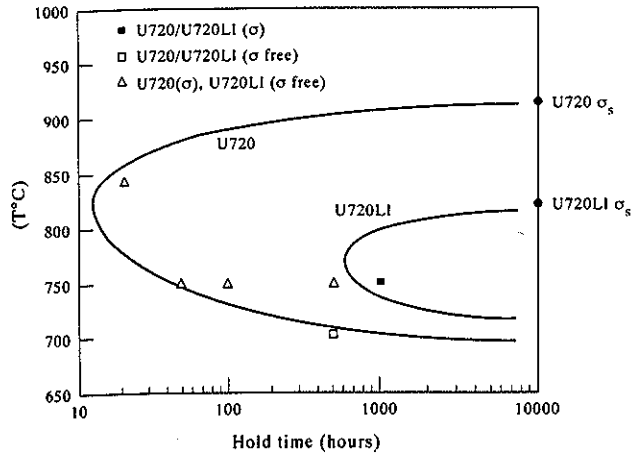

Figure 10.48 TTT diagrams for U720 and U720LI based on calculated σ-solvus temperatures.

References are listed on pp. 402–408.

10.6.1.2 The effect of Re on TCP formation in Ni-based superalloys. As gas turbine engines are designed and manufactured to work at higher and higher thrust-to-weight ratios, the temperature capability of most components has had to be increased. This has applied particularly to the high-pressure (HP) turbine blades where the development of new alloys has followed lines associated both with the development of microstructure and new chemistries. HP turbine blades are now commonly single-crystal materials where the grain boundaries have been removed by novel casting techniques. HP blades have also seen the development of alloy variants which typically contain Re at levels of between 2 and 6wt%. Because Re is such a heavy element, this relates to a small addition in atomic terms, but the effect on properties such as creep and strength is pronounced. Re also has a profound effect on the temperature at which TCPs are observed, raising this substantially (Darolia *et al.* 1988, Erickson *et al.* 1985). The reason for this is not readily understood in terms of a PHACOMP approach (Darolia *et al.* 1988), and it therefore is interesting to look at how CALPHAD methods can deal with an element like Re.

CMSX-4 is a second generation single crystal superalloy and typically has the composition Ni–6.3Cr–9Co–0.6Mo–6W–6.5Ta–3Re–5.6Al–1Ti–0.1Hf (in wt%). Figure 10.49 shows a calculated phase % vs temperature plot for this alloy and most aspects of its phase behaviour appear well matched. The high-temperature TCP phase is the *R* phase, in excellent agreement with the work of Proctor (1992) and its predicted composition is also in good agreement with Proctor (1992), with W and Re in almost equal proportions (~35wt% each). It is clear that the partitioning of Re

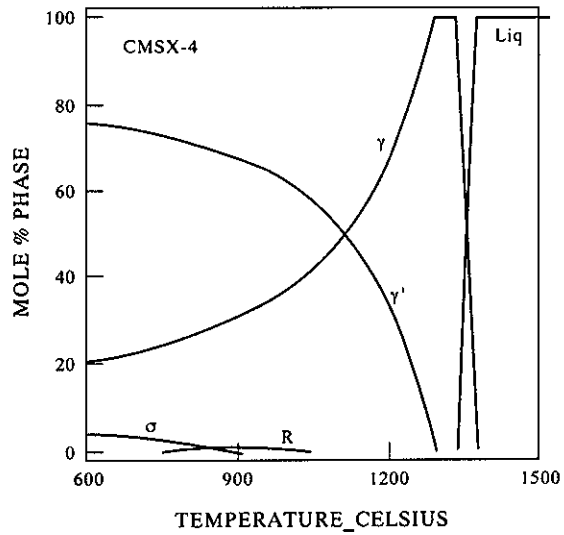

Figure 10.49 Calculated mole % phase vs temperature plot for a CMSX-4 Ni-based superalloy.

to the R phase is particularly strong and even stronger in σ, where levels can reach 45wt%. Although the formation of TCP phases is clearly enhanced because they are so rich in Re, their amounts in the alloy are restricted by the total level of Re, in this case only 3wt%. Therefore, the amounts of σ and R never rise to catastrophic levels as was evident in the previous example of U720. This has the corollary that Re-containing single-crystal alloys, such as CMSX-4, may be relatively tolerant to TCP formation even though their temperatures of formation can be high.

The sensitivity of TCP formation to Re can be further emphasised by examining what happens to CMSX-4 when the Re level is reduced by ½ to 1.5wt% accompanied by a corresponding increase in W level. For this case the solvus temperature falls by some 50°C. A similar exercise of replacing Re with W was performed by Darolia *et al.* (1988) and their observed variations in the start temperature of TCP formation are in reasonable accord with this.

It is also evident that there is a complex interplay between the three main TCP phases, σ, R and P, with μ occasionally being observed (Darolia *et al.* 1988, Proctor 1992, Walston *et al.* 1996). To examine this more closely, calculations were made for CMSX-4 by alternatively suspending two of the three main TCP phases and calculating the behaviour of the alloy with just one of the phases allowed to form at any one time (Fig. 10.50). The solvus temperatures for R, P and σ respectively were calculated as being close to each other at 1045°, 1034° and 1026° respectively, and the R and P phases are particularly close in stability over the whole temperature range. It is clear, therefore, that the interplay between the various TCP phases will be sensitive to the alloy composition and indeed changes in Re, W and Cr levels will cause either σ, R or P to become the dominant TCP phase.

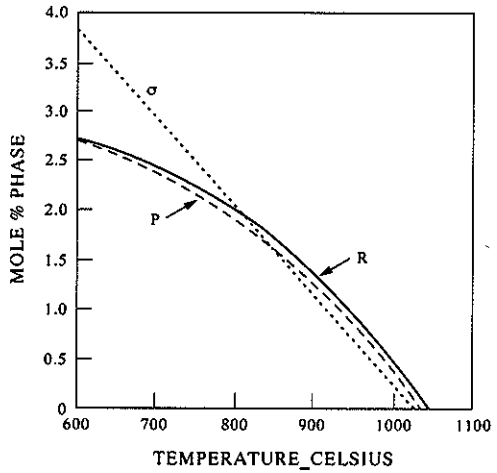

Figure 10.50 Calculated mole % phase vs temperature plot for a CMSX-4 Ni-based superalloy with only one TCP phase allowed to form at any one time.

References are listed on pp. 402–408.

10.6.2 Complex precipitation sequences

10.6.2.1 7000 series Al-alloys. Probably the most complex type of Al alloys are the 7000 or 7XXX series. These are based on the Al–Cu–Mg–Zn quaternary system and hardening reactions are based on one or more of three phases: (1) η, which is based on the binary Mg–Zn Laves compound but also exists in Al–Cu–Mg; (2) T_AlCuMgZn, which exists in both the Al–Cu–Mg and Al–Mg–Zn systems; and (3) S_Al_2CuMg (as in an AA2024 alloy). In these alloys it is the Zn/Mg ratio which is considered most critical in deciding the type of precipitation reaction which takes place. It should be noted that in practice an alloy such as AA7075 achieves maximum hardness due to the precipitation of the metastable η' phase which is structurally related to η. Also, both the T_AlCuMgZn and S_Al_2CuMg phases can form similar metastable hardening phases. At present, thermodynamic descriptions for these phases do not exist but, because of the inherent relationship between the metastable and stable forms of the compounds, it is reasonable to expect that the metastable precipitate which forms will be closely related to the respective stable precipitate which predominates in the alloy. Also, a number of important questions connected with processing are directly related to the stable forms; for example, solution temperatures and intermediate heat-treatment temperatures and their formation during non-equilibrium solidification. It is therefore instructive to look at a series of calculations for 7XXX alloys to observe how the calculated diagrams vary as the composition of the alloys is changed.

Figures 10.51a–d show the precipitation of the three major hardening phases, η, T and S, as well as ε-AlCrMnMg and Mg_2Si, for a series of high-strength 7000 series alloys with Zn:Mg ratios as given in Table 10.1. For simplicity, other phases which may appear, such as Al_6Mn, α, etc., have not been included. AA7049 represents the highest Zn:Mg ratio and also gives one of the highest values for the total percentage (Zn+Mg) total. In this case the hardening phase is almost completely η and its level rises to a maximum of 6% in molar units. As the Zn:Mg ratio is reduced from 3.1 to 2.7 in the AA7050 alloy the competition between T and η is still won easily by η but, due to the high levels of Cu in this alloy, it will also be significantly prone to the formation of S_Al_2CuMg. The 7075 alloy has a lower Zn:Mg ratio of 2.2 and although still predominantly hardened by η, some T phase

Table 10.1 Composition and Zn/Mg ratio of various 7XXX alloys (after Polmear 1989). Values for Si, Fe and Mn relate to maximum values

Alloy	Si	Fe	Cu	Mn	Mg	Zn	Cr	Zn/Mg
AA7049	0.25	0.35	1.5	0.2	2.5	7.7	0.15	3.1
AA7050	0.12	0.15	2.3	0.1	2.3	6.2	0.04	2.7
AA7075	0.4	0.5	1.6	0.3	2.5	5.6	0.23	2.2
AA7079	0.3	0.4	0.6	0.2	3.3	4.3	0.18	1.3

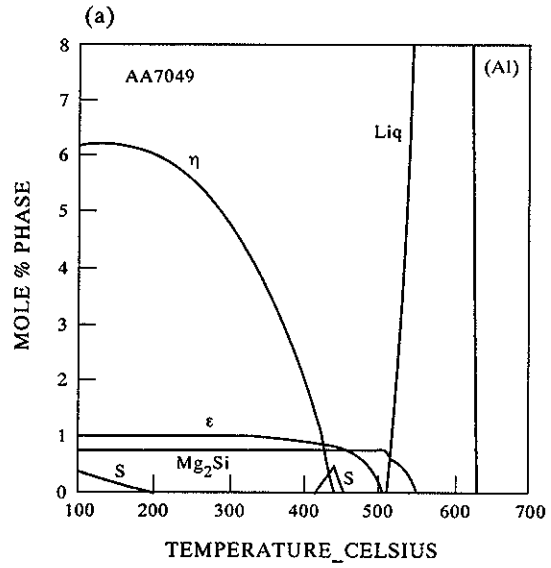

Figure 10.51 Calculated mole % phase vs temperature plots for 7XXX series Al-alloys. (a) AA7049, (b) AA7050, (c) AA7075 and (d) AA7079.

References are listed on pp. 402–408.

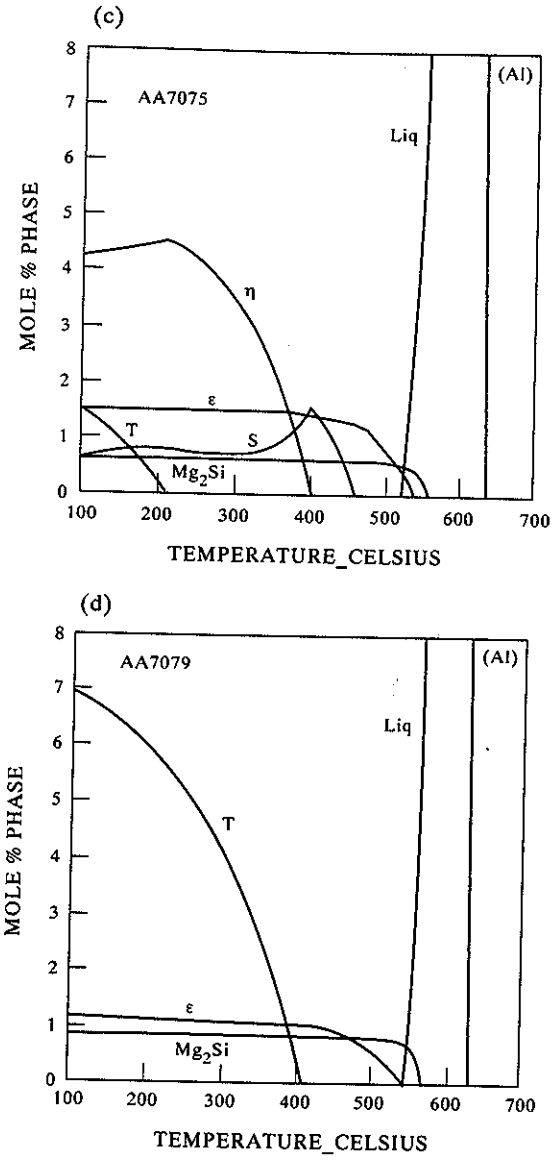

Figure 10.51 (c) and (d).

begins to appear below 200°C. It is also noteworthy that the level of *S* phase is reduced. Both of these effects are due to the reduction of Cu levels in AA7075. This means that less *S* phase is formed, which releases Mg, and effectively means that more Mg is available in the alloy. We are therefore forced to consider the concept of an *effective* Zn:Mg ratio which is potentially affected by the level of Cu in the alloy. The final alloy, AA7079, has the lowest Zn:Mg ratio of 1.3, well below a value of 2 which is considered the critical point at which the *T* phase is favoured. As would be expected, the main precipitation now occurs by the *T* phase with no predicted formation of η and no *S* phase because of the effective absence of Cu.

As stated previously, the predominant hardening in these alloys may be controlled by the metastable forms of the various phases, but it is clear that the calculations have allowed a quick scan to be made of the major types of equilibrium precipitates and this must have a significant bearing on the formation of the metastable forms. Furthermore, the role of Cu can be better understood as can also the effect of the various minor elements on the 'insoluble' compounds. It is also interesting to note the predicted formation of the ε-AlCrMnMg phase with the addition of Cr. In AA7075 it helps retard recrystallisation during the high-temperature heat treatment for this alloy and is, therefore, beneficial.

10.6.2.2 (Ni, Fe)-based superalloys. Ni,Fe-based superalloys, such as 718, can behave in a complex fashion, which is associated with the formation of various carbides and the interplay between three major precipitated phases; δ based on Ni_3Nb, γ' based on Ni_3Al and a metastable phase γ'' which is related to the δ phase. Inconel® 625 (IN625) was the prototype for the Nb-hardened NiFe-type superalloys and it is instructive to look at the complex precipitation phenomena which occur in this alloy which has the composition Ni–21.5Cr–9Mo–3.6Nb–5Fe–0.2Al–0.2Ti–0.05C (in wt%).

Figures 10.52(a,b) show phase % vs temperature plots for a standard IN625 alloy. It is predominantly strengthened at low temperatures by the formation of δ and is characterised by the formation of three types of carbide, MC, M_6C and $M_{23}C_6$. It is further unstable with respect to both σ and μ at low temperatures. This behaviour shows that the alloy lies close to a 'boundary' which is controlled by the Mo/Cr ratio where, at lower Mo/Cr ratios, the alloy would contain MC and the more Cr rich phases $M_{23}C_6$ and σ, while at higher Mo/Cr ratios the alloy would contain MC and the more Mo-rich phases M_6C and μ.

The temperature range of formation of the various carbides and the solvus temperatures of δ are well established (Ferrer *et al.* 1991, Vernot-Loier and Cortial 1991) and the calculated diagram is in excellent agreement with this experimental information. However, during processing it is usually the γ'' phase which is formed instead of δ. This is due to much faster transformation kinetics of this phase and hardening Ni,Fe-based superalloys is usually due to a combination of γ' and γ''.

References are listed on pp. 402–408.

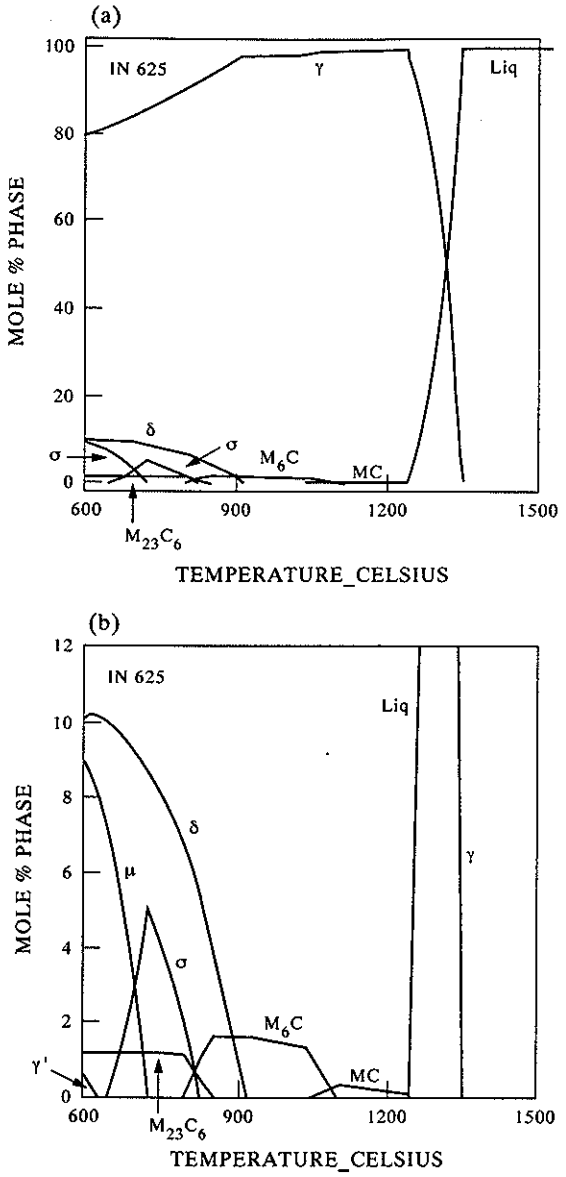

Figure 10.52 (a) Calculated mole % phase vs temperature plots for an IN625 Ni-based superalloy. (b) Expanded region of Fig. 10.50(a).

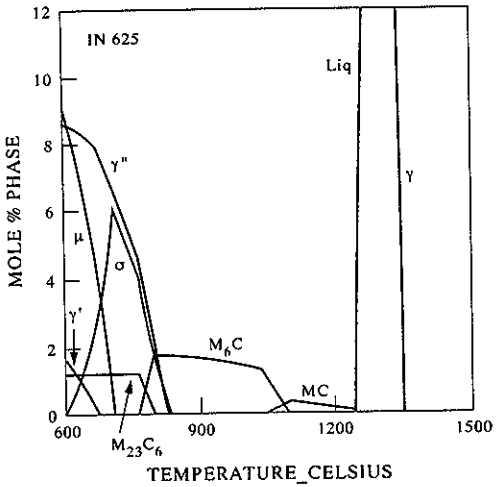

Figure 10.53 Calculated mole % phase vs temperature plots for an IN625 Ni-based superalloy with the δ phase suppressed.

This can be modelled by suspending the δ phase from the calculations and Figure 10.53 shows the subsequently calculated phase % plot. Again, the solvus temperature for γ'' is well matched with a consequent increase in the γ' solvus temperature of some 50°C.

10.6.2.3 Micro-alloyed steels. In the past 20 years the strength and toughness of high-strength low-alloy (HSLA) steels has improved considerably through micro-alloying additions. These additions, typically Ti, Nb and V, form stable carbonitrides which help both by reducing grain growth during the high-temperature annealing process and by precipitation hardening at lower temperatures. Similar effects occur with so-called interstitial-free (IF) steels. Modelling work on such alloys has been reasonably extensive (Zou and Kirkaldy 1992, Houghton 1993, Akamatsu *et al.* 1994) and, although at first sight the formation of such carbonitrides may appear relatively straightforward, there is an internal complexity which should not be underestimated.

In essence two types of carbonitride are formed in a Ti,Nb-hardened micro-alloyed steel. At high temperatures a predominantly TiN-rich carbonitride is formed. However, on cooling to lower temperatures a predominantly NbC-rich carbonitride also precipitates. Both carbonitrides are based on the NaCl structure and form part of a continuum usually described by a formula such as $(Ti_xNb_{1-x})(C_zN_{1-z})$. This can be expanded to include elements such as V and Ta, so the formula becomes $(Ta_xTi_yNb_zV_{1-x-y-z})(C_zN_{1-z})$. The formation of two types of carbonitride can be considered due to 'phase separation' and Fig. 10.54 shows a projected miscibility gap for the simple case of $(Ti_xNb_{1-x})(C_zN_{1-z})$ from Akamatsu *et al.* (1994). If the composition of the carbonitride lies outside the miscibility gap, simple single-phase carbonitrides form. But as the temperature is lowered the miscibility gap extends over much of the composition space and breakdown to TiN-rich and NbC-rich phases is possible.

In reality, the modelling issues are even more interesting as the NaCl carbonitride structure is formed by the filling of the octahedral sites of austenite and there is actually a continuum between austenite and the carbonitride phase. The duplex precipitation is therefore occurring by a breakdown of an Fe-rich phase to first form a TiN-rich carbonitride which subsequently undergoes further separation. Providing the f.c.c._A1 phase is modelled correctly, the calculation can be made by considering only two phases, the ferritic b.c.c._A2 and the f.c.c._A1 phase which then separates to form the austenite, the TiN-rich carbonitride and the NbC-rich carbonitride phases. This has the advantage that non-stoichiometric effects in the carbonitride can also be considered and the formula becomes $(Fe_wTi_xNb_{1-w-x})(C_yN_zVa_{1-y-z})$. Figure 10.55 shows a calculation for a micro-alloyed steel with a composition after Zou and Kirkaldy (1992) and the formation of the two types of carbonitride is predicted to form, as is observed in practice.

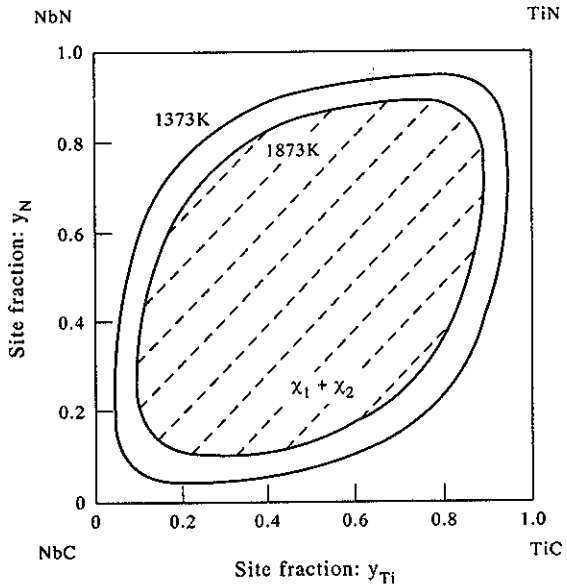

Figure 10.54 Projected miscibility gap for the case of $(Ti_xNb_{1-x})(C_zN_{1-z})$ from Akamatsu *et al.* (1994).

References are listed on pp. 402–408.

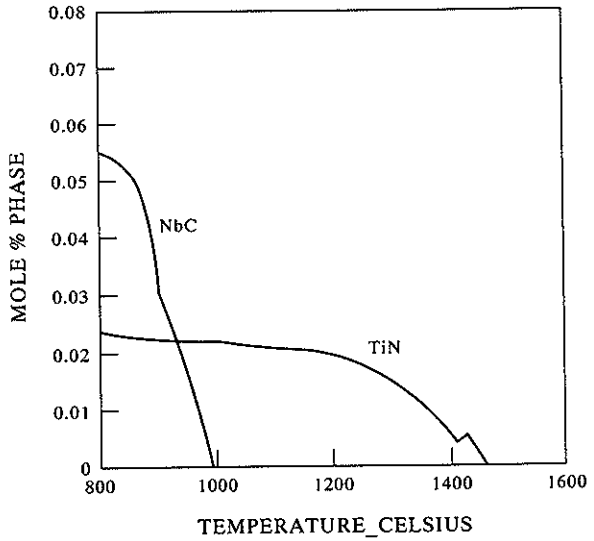

Figure 10.55 Calculated mole % vs temperature plot for a micro-alloyed steel showing precipitation of TiN- and NbC-based carbides.

10.6.3 Sensitivity factor analysis

An interesting and important corollary of CALPHAD calculations is to predict sensitivity factors for various important material properties, such as liquidus and solidus temperature, solid state transus temperatures, heat-treatment windows, etc. These can then be utilised both in alloy design and in production of alloys or components.

10.6.3.1 Heat treatment of duplex stainless steels. An excellent example of the application of CALPHAD methods to sensitivity analysis is in the work of Longbottom and Hayes (1994) on duplex stainless steels. These materials contain a mixture of austenite and ferrite, usually with a 50:50 proportion of each phase, and are produced by suitable heat treatment, typically in the range 1050–1150°C. The amount of austenite and ferrite is critically controlled by the composition of the alloy which dictates the temperature where there is the ideal 50:50 ratio. The particular alloy of interest in their study was a Zeron 100 alloy with the nominal composition Fe–25Cr–3.5Mo–6.5Ni–1Mn–1Si–0.75Cu–0.75W–0.25N–0.15C (in wt%). Using original experimentation, Longbottom and Hayes (1994) confirmed that the correct austenite levels, as a function of temperature, were calculated for a set of four Zeron 100 variants. Figure 10.56 shows the agreement between their experimental work and calculations and, except for three cases, the calculations agree within the error bar of the measurements.

References are listed on pp. 402–408.

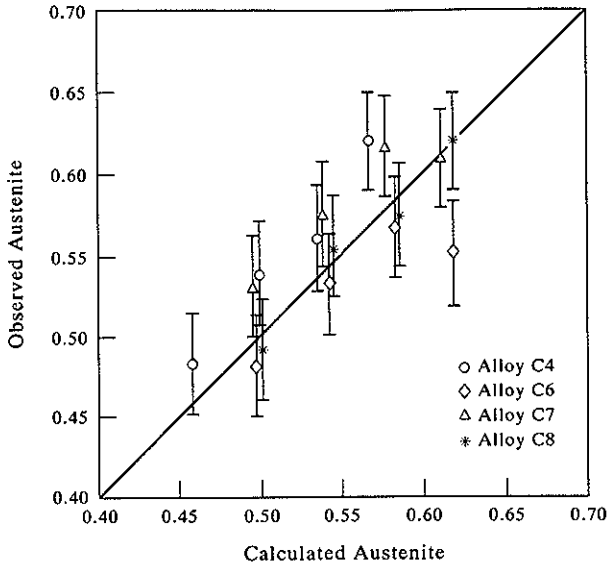

Figure 10.56 Comparison between thermodynamically calculated and experimentally observed amounts of austenite in Zeron 100 duplex stainless steels (Longbottom and Hayes 1994).

Rather than utilise a full thermodynamic calculation for their final sensitivity analysis, they fitted their calculated results to a formula which could be used within the composition specification range of Zeron 100 alloys, such that the fraction of austenite, f^{γ}, was given by

$$\begin{aligned} f^{\gamma} = {} & +2.2 - 1.39 \times 10^{-3} T \\ & + (1.35 \times 10^{-3} T - 0.78)\%\mathrm{C} + (1.30 \times 10^{-5} T - 0.037)\%\mathrm{Cr} \\ & - (2.44 \times 10^{-6} T - 0.099)\%\mathrm{Cu} - (5 \times 10^{-5} T - 0.061)\%\mathrm{Mn} \\ & - (3.08 \times 10^{-6}, T + 0.0081)\%\mathrm{Mo} + (1.56 \times 10^{-3} T - 1.40)\%\mathrm{N} \\ & - (3.97 \times 10^{-5} T - 0.11)\%\mathrm{Ni} + (3.32 \times 10^{-4} - 0.61)\%\mathrm{Si} \\ & + (2.11 \times 10^{-5} - 0.038)\%\mathrm{W}. \end{aligned} \tag{10.1}$$

Figure 10.57 compares the results obtained using this formula with the thermodynamic calculations, while Fig. 10.58 shows the comparison with experimental volume fractions. This formula can now be written in simple software code to provide an almost instant answer to the temperature at which heat treatment will give the ideal 50:50 ratio of austenite to ferrite.

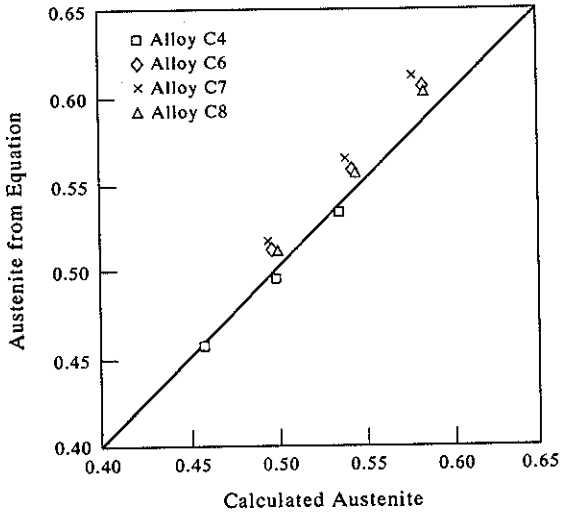

Figure 10.57 Comparison between austenite amounts calculated thermodynamically and calculated using Eq. (10.1) (Longbottom and Hayes 1994).

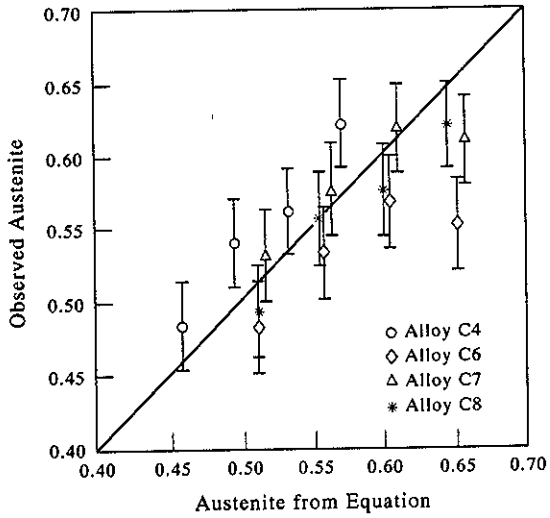

Figure 10.58 Comparison between experimental austenite amounts and those calculated using Eq. (10.1).

References are listed on pp. 402–408.

10.6.3.2 σ phase in Ni-based superalloys. Section 10.6.1.1 showed how CALPHAD calculations could be used to predict σ formation in Udimet 720 and 720LI alloys. A corollary is to calculate how the σ-solvus varies as the contents of the different elements are altered, and Fig. 10.59 shows such variations in σ-solvus temperature for U720LI as each element is changed within its nominal specified composition limits. It is interesting to note that the greatest sensitivity is to Al, with a Ti sensitivity similar to that of Cr. This is because additions of Al and Ti increase the levels of γ' in the alloy and reject σ-forming elements such as Cr, Mo and W into the γ phase. As the amount of γ decreases there is a significant increase in concentration of these elements in γ, which leads to higher susceptibility to σ formation. Taking the information in Fig. 10.59 it is now possible to define σ-sensitivity factors for each of the elements with a simple mathematical formula, as in the previous section. This can then be used to monitor σ susceptibility of different heats during alloy production, replacing PHACOMP methods. Such sensitivity factors can be defined for all types of production features where phase equilibria are important for Ni-based superalloys, for example γ' heat-treatment windows, levels of γ' at heat-treatment or forging temperatures, solidus and liquidus temperatures, etc.

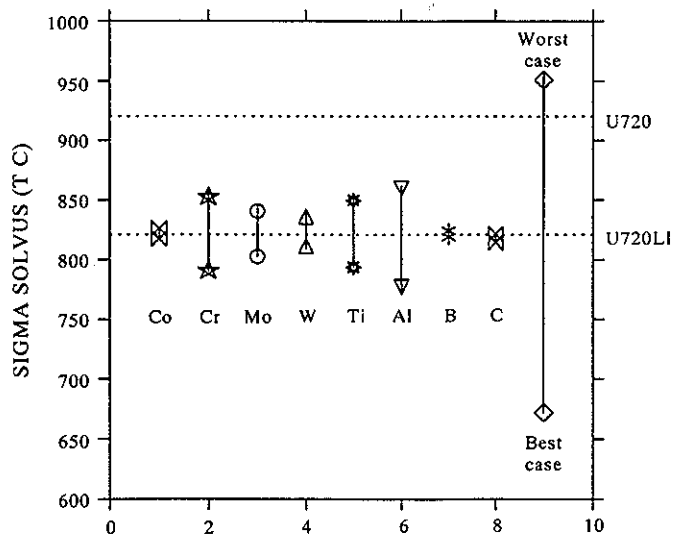

Figure 10.59 Variation in calculated σ-solvus temperature as elements in U720LI change between maximum and minimum specified limits.

10.6.3.3 Liquid-phase sintering of high-speed M2 steels. High-speed steels, which typically contain at least seven elements, can be produced in a variety of ways, for example by casting, by water or gas atomisation with subsequent hot compaction of the atomised powder, and by liquid-phase sintering. The latter provides a production route whereby the steel can be produced directly to the correct shape. The process relies on there being sufficient liquid to infiltrate the pores of a powder compact and produce densification, but not too much, as this would cause the compact to lose structural strength and distort. A reasonable level for liquid-phase sintering is approximately 10% of the volume. It is also critical that the volume of liquid is fairly insensitive to fluctuations in temperature in the furnace, i.e., dV_{liq}/dT is as small as possible, otherwise the sensitivity of the process to fluctuations in temperature control, or the intrinsic variations in temperature within the furnace itself, makes the process uncontrollable.

Figure 10.60 shows a phase % vs temperature plot for an M2 steel with a composition (in wt%) of Fe–6.2W–5.1Mo–4.2Cr–1.85V–0.3Si–0.8C. The alloy is characterised by the formation of two types of carbide, M_6C, which is the predominant form, and MC. The calculated melting temperature is close to that observed for such alloys and the amount of M_6C and MC is also in good agreement with experimental observation (Hoyle 1988). Chandrasekaran and Miodownik (1989, 1990) and Miodownik (1989) examined M2 steels, with particular emphasis on the effect of increasing V levels to increase the formation of the V-rich MC carbide. Figure 10.61 shows the change in behaviour of M2 when the V level is increased from 1.85 to 2.5wt%, calculated using Fe-DATA (Saunders and Sundman 1996). The MC carbide is stabilised as expected, but α is also stabilised and becomes involved in a fairly complex reaction scheme with the liquid, γ, M_6C and MC. Both of these effects are qualitatively expected, but now the CALPHAD route enables calculations to be made for the amount of liquid as a function of temperature. Figure 10.62 shows such calculations as V levels are raised from 1.75% to 2.5% and the increase in solidus temperature with increasing V addition reflects well the experimental measurements quoted by Chandrasekaran and Miodownik (1989). It can now be seen that the slope of the liquid curve is flat for the lower levels of V, i.e., dV_{liq}/dT is small, but as the V levels reach 2.5wt%V, the slope becomes steep. Clearly there will be a limit around this composition at which the alloy will become difficult to fabricate by liquid-phase sintering.

10.6.4 Intermetallic alloys

Intermetallic alloys (compounds) are becoming of increasing interest as materials which possess significantly enhanced high temperature capabilities compared to many conventional metallic alloys. However, they suffer intrinsic problems associated with low-temperature ductility and fracture toughness. Two types of

References are listed on pp. 402–408.

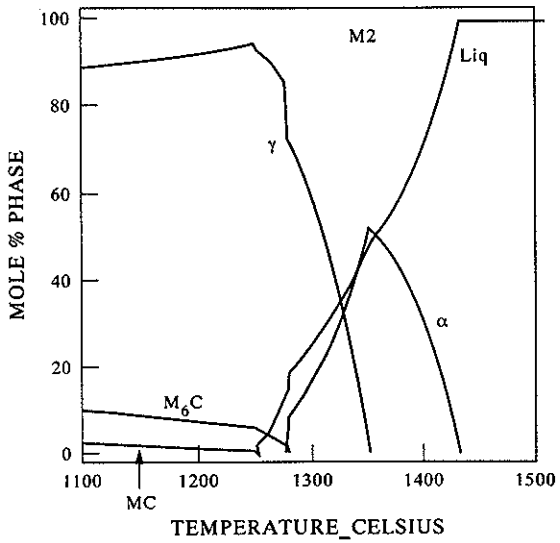

Figure 10.60 Calculated mole % phase vs temperature plot for an M2 steel with normal V level.

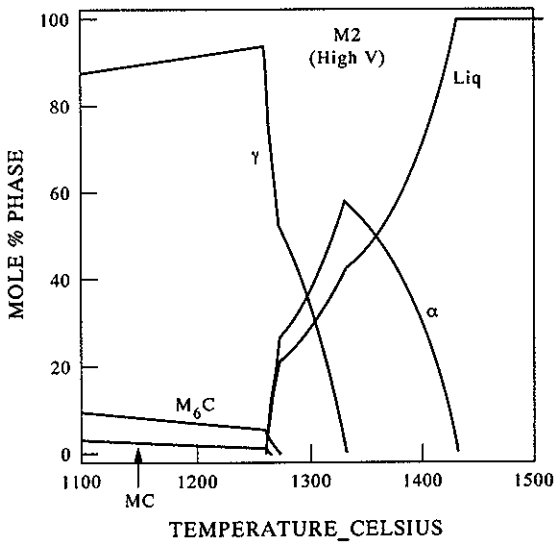

Figure 10.61 Calculated mole % phase vs temperature plot for an M2 steel with high V level.

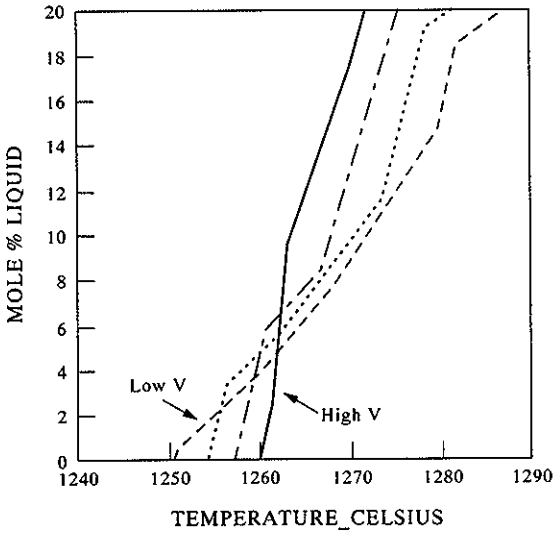

Figure 10.62 Calculate mole % liquid vs temperature plots for an M2 steel as V levels are changed between 1.75 and 2.5wt%.

intermetallic alloys have attracted wide attention, those based on NiAl and those on TiAl. The next two sections describe work on both types of alloy.

10.6.4.1 NiAl-based intermetallic alloys. Phase-diagram studies have been used extensively in NiAl-based alloys as a method of designing microstructures. NiAl is difficult to prepare as a binary alloy with reasonable levels of ductility and fracture toughness. Therefore considerable effort has been placed in designing microstructures which might reduce this inherent brittleness. An approach has been to make alloy additions to NiAl so that it forms a two-phase structure with a more ductile phase, such as the f.c.c. Ni–Fe-based solid solution, γ, (Ishida *et al.* 1991), or even γ' based on Ni_3Al (Kainuma *et al.* 1996). This has been shown to produce high levels of ductility for such materials but, unfortunately, the process of ductilisation by a softer second phase does lead to a degradation of intrinsic strength and high-temperature creep capability. Another approach to designing NiAl alloys has been to produce multi-phase structures containing NiAl + other intermetallic compounds such as the Heusler-type phase Ni_2AlTi and γ' (Yang *et al.* 1992a, b). These alloys are less ductile but have significantly higher yield strengths and potentially enhanced creep properties.

The approach of Ishida *et al.* (1991) and Kainuma *et al.* (1996) utilised both experimentally determined and calculated diagrams for Ni–Al–Fe (Fig. 10.63) to

References are listed on pp. 402–408.

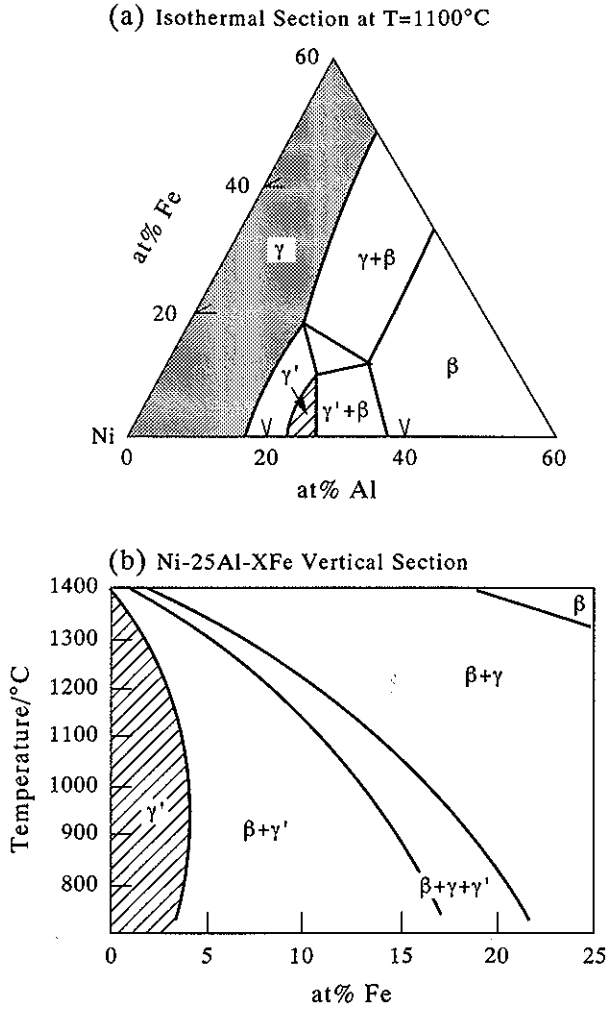

Figure 10.63 Phase equilibria in the Ni–Al–Fe system from Kainuma *et al.* (1996).

define compositions whereby various mixtures of NiAl and γ/γ' could be produced. These authors optimised their alloys on the basis of the amounts of the various phases as well as their microstructure. In their case, the initial microstructure was an $L1_0$ martensite formed by transformation of the β phase on cooling. By using a series of heat treatments and varying the composition of the alloy they were able to design three distinct types of microstructure (Fig. 10.64) and successfully produce

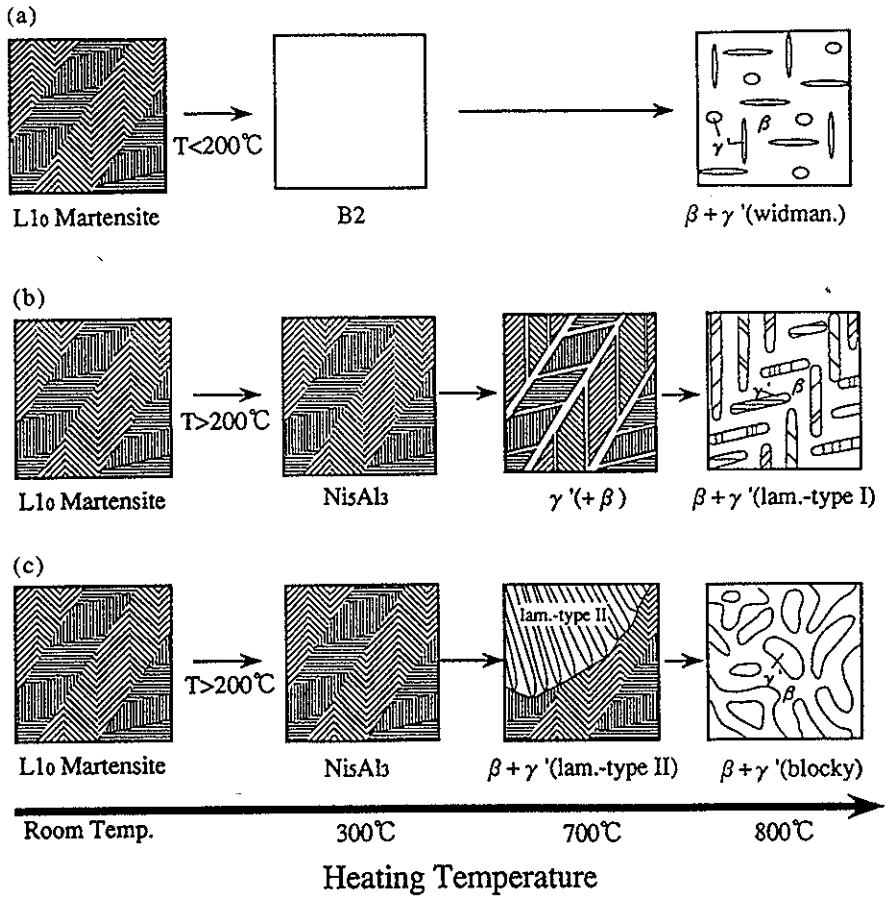

Figure 10.64 Schematic illustrations showing the microstructural evolution of three kinds of $\beta + \gamma'$ microstructures; widmanstätten, type 1 lamellar and blocky type 2 lamellar structures in Ni–25Al–(a)18Fe, (b)15Fe and (c)13Fe alloys.

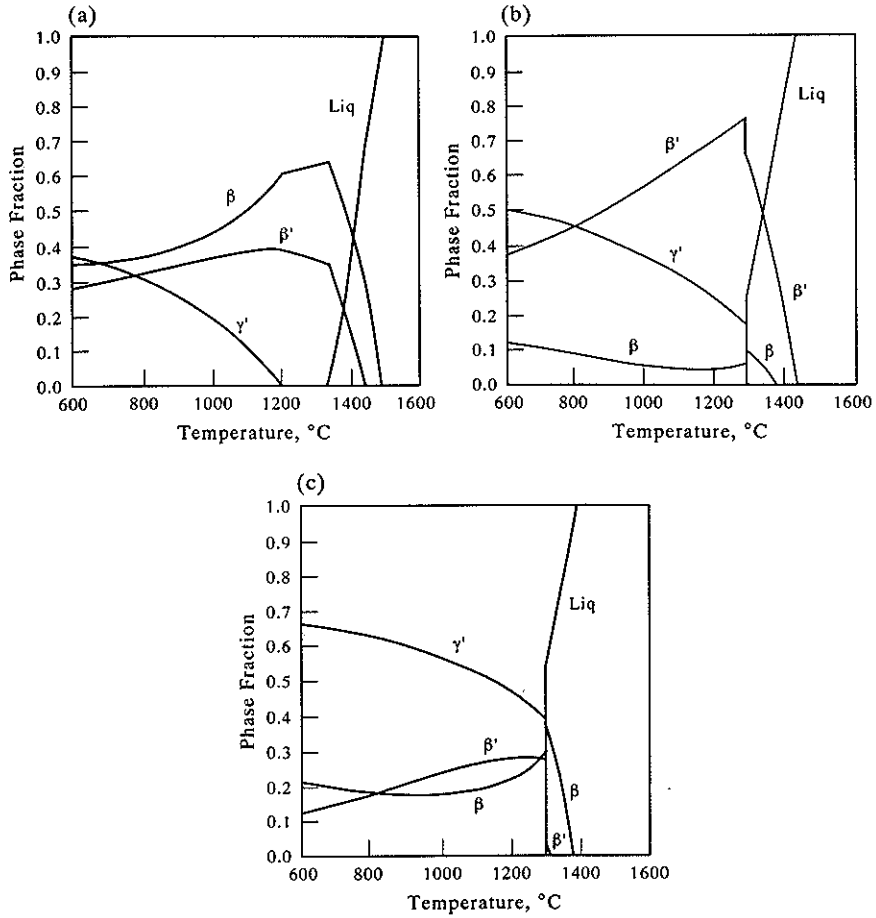

Figure 10.65 Calculated mole % phase vs temperature plots for Ni–Al–Ti intermetallic alloys. (a) Ni–28Al–12Ti, (b) Ni–22Al–15Ti and (c) Ni–20Al–13Ti.

NiAl-based alloys with ductilities as high as 10% in tension and strengths in the region of 750–1000 MPa.

Yang *et al.* (1992a, b) also utilised a combination of experiment and calculation to critically determine the phase region for the β-NiAl, γ'-Ni_3Al and β'-Ni_2AlTi phases. The philosophy of their approach was to produce an alloy with high levels of β and β', as mixtures of these phases had been shown to have enhanced creep resistance in comparison to the monolithic phases themselves (Polvani *et al.* 1976). The combination of experiment and calculated phase % vs temperature plots (Figs. 10.65(a–c)) allowed precise microstructures to be defined and subsequently produced in candidate alloys. In these alloys the microstructure was as much controlled by the solidification mechanism as by any solid state transformation and, as such, the calculations were invaluable as they could be used to predict solidification patterns. Alloys produced as part of this programme had high compressive yield stresses, in the range of 1000–2000 MPa, and, although the alloys still had quite low tensile ductility, there is a significant enhancement in ductility due to the generation of dislocations at interphase boundaries.

References are listed on pp. 402–408.

10.6.4.2 TiAl-based intermetallic alloys. Alloys based on the γ-TiAl compound are still very much in the early stages of development. Commonly used variants such as Ti–48Al–2Mn–2Cr and Ti–48Al–2Mn–Nb (at%) are quaternary in nature and it is only recently that alloys of a multi-component nature have been developed. As alloy development has progressed, increasingly complex behaviour has been observed and changes in transformation behaviour can now be tracked using a recently developed TiAl database (Saunders 1997b). All alloys are based on the γ-TiAl compound of Ti–Al and Fig. 10.66 shows the calculated diagram for the binary system Ti–Al. Alloys usually contain between 43–50at%Al and, for the most part, contain α_2-Ti_3Al as well as γ-TiAl. They are usually heat treated in the high-temperature, single-phase α-phase region, or just below it, before cooling when the α phase decomposes to a microstructure which exhibits a fine lamellar structure of transformed γ-TiAl with fine laths of α_2-Ti_3Al.

Figure 10.67 shows a mole% phase vs temperature plot for a Ti–48Al–2Mn–2Nb alloy of nominal composition; variations of this alloy with Al in the range 45–48at% are commonly used. It is a straightforward α_2/γ alloy which can be heat treated in the α condition before transforming on cooling to $(\alpha_2 + \gamma)$ and very much exhibits the prototype microstructure for the early type of alloys.

The replacement of Mn by Cr in the Ti–48Al–2Cr–2Nb alloy (Fig. 10.68) causes the predicted onset of instability with respect to a Cr-rich B2 phase. This in good accord with experimental observations in alloys of this type (Fuchs 1995, Kelly and Austin 1996) and at low temperatures there is also a potential for the formation of

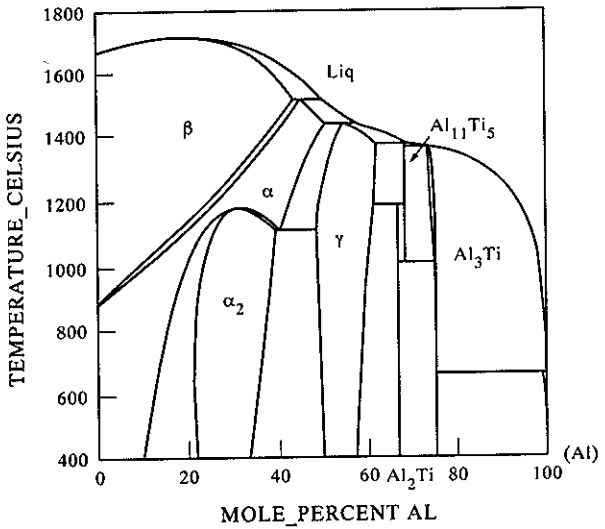

Figure 10.66 Calculated Ti–Al phase diagram.

References are listed on pp. 402–408.

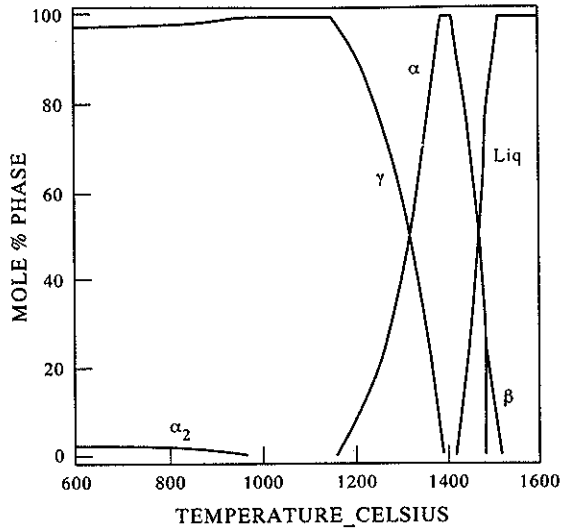

Figure 10.67 Calculated mole % phase vs temperature plot for a Ti–48Al–2Mn–2Nb alloy.

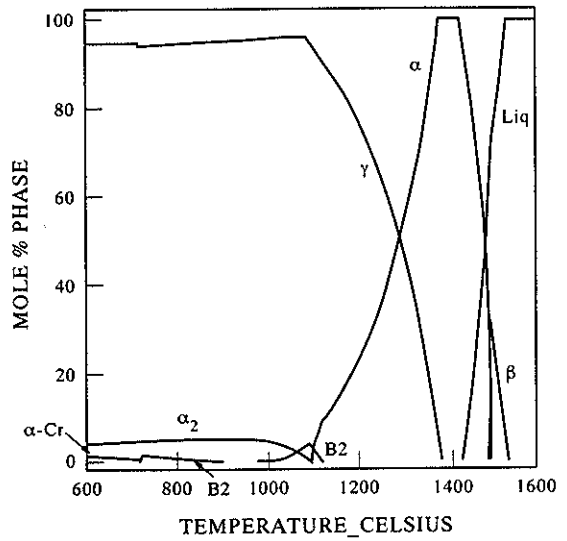

Figure 10.68 Calculated mole % phase vs temperature plot for a Ti–48Al–2Cr–2Nb alloy.

Table 10.2. Some recent γ-TiAl-based alloys with comparison between experimentally observed and calculated α-transus temperatures

Alloy	α-transus (exp.)	α-transus (calc.)	Reference
Ti–48Al–2Cr–2Nb	1364	1357	Fuchs (1993)
Ti–49.5Al–1.1Mn–2.5Nb	1436	1425	Lombard *et al.* (1992)
Ti–47Al–2.5Nb–1Cr–1V	1350	1357	Kim (1992)
Ti–46.7Al–3Nb–1W	1350	1353	Bhowal *et al.* (1995)
Ti–48Al–2Nb–2Cr–1W	1358	1371	Fuchs (1995)
Ti–47Al–1.5Cr–0.5Mn–2.6Nb–0.15B	1365	1367	Kim (1995)
Ti–47Al–2Nb–1Mn–0.5W–0.5Mo–0.2Si	—	1366	Seo *et al.* (1995)

almost pure Cr. Newer alloys have centred around the substitution and addition of elements to the 48–2–2-type alloys and have compositions of the type shown in Table 10.2, which also gives comparisons for experimentally observed and calculated α-transus temperatures.

It is noticeable that heavy elements such as W and Ta are now being increasingly used and that alloys are subsequently becoming more prone to formation of the B2 phase. This is seen for example in alloys such as Ti–48Al–2Nb–2Cr–1W, and their variants (Fuchs 1995). One of the most complex alloys developed so far is Ti–47Al–2Nb–1Mn–0.5W–0.5Mo–0.2Si. However, although truly multi-component in nature, the total refractory metal addition to a basic Ti–Al alloy is still only 4at%. The microstructure of this alloy consists of second-phase particles enriched in Mo and W and there is also evidence for silicides (Seo *et al.* 1995). Figure 10.69 shows the calculated phase % vs temperature plot for this alloy; the alloy is predicted to be unstable with respect to a B2 phase enriched in Mo and W, and Ti_5Si_3 will form below 1020°C. The calculation also predicts that the alloy may become unstable with respect to W precipitation at low temperatures.

It is clear that as these alloys have become more highly alloyed, the simple prototype concept of an α_2/γ microstructure is having to be modified to take into account borides, silicides and the B2 phase. It is now possible to understand the role of the various elements in promoting these phases and also to design with them in mind. For example, the B2 phase can inhibit grain growth if it is present in the high-temperature α-phase field. This appears somewhat analogous to conventional Ti alloys, where some small amounts of α in β grain boundaries during processing and help prevent catastrophic grain growth during forging, but the role of the phases is completely reversed.

10.6.5 Alloy design

Most of the previous examples show that CALPHAD calculations can enhance knowledge of the general phase behaviour of alloys when a suitable thermodynamic

References are listed on pp. 402–408.

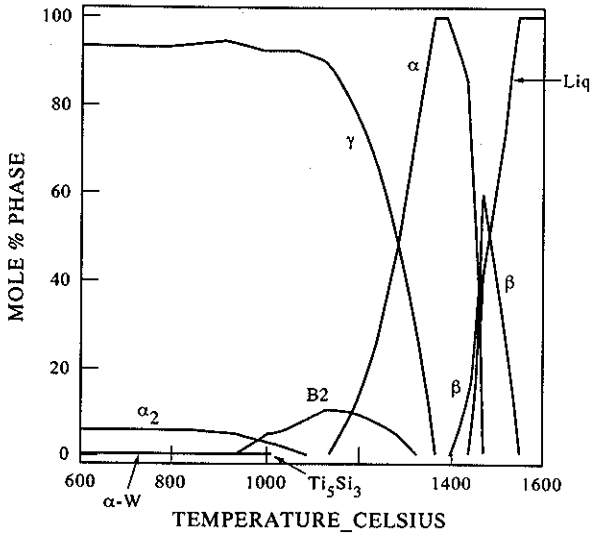

Figure 10.69 Calculated mole % phase vs temperature plot for a Ti–47Al–2Nb–1Mn–0.5W–0.5Mo–0.2Si alloy.

database is available. However, it is also interesting to look at some CALPHAD-based work where the main aim has been to help design or optimise some specific feature, or combinations of features, which are affected by phase behaviour. Such features may be associated with a physical property such as modulus and magnetism, a mechanical property such as strength, a chemical property such as corrosion resistance or some more complex combination which might effect a property such as weldability. The best examples centre around Fe-based materials, which probably relates to historical reasons as Fe-based systems were one of the first types of alloy to be thermodynamically characterised in any great detail. However, it is clear that once good thermodynamic characterisations are available the use of CALPHAD methods need not be limited to any particular material type (Miodownik 1993).

10.6.5.1 Magnetic materials. The value of CALPHAD calculations for magnetic alloys has been demonstrated for Fe–Cr–Co-based alloys, where alloys with improved magnetic properties were made by designing their composition and heat-treatment temperature to lie in a miscibility caused by magnetic forces (Nishizawa *et al.* 1979a, Homma *et al.* 1981, Ishida and Nishizawa 1991). Inden (1987) has described in detail the background to the production of such hard magnets which can be summarised as follows.

A good design for a hard magnetic material is to have small, elongated particles,

aligned and magnetised along their axis, embedded in a paramagnetic matrix. One of the easiest ways to produce such a microstructure is by some form of precipitation reaction, where the size of the particles can be controlled by heat treatment. This then leaves the problem of producing the requisite shape and alignment of the particles which leads to a further prerequisite that the precipitate/matrix interface must have a low energy. It is not always possible to produce 'ideal' rod shapes, but precipitates with a more plate-like morphology can also be aligned by applying a magnetic field during the precipitation process.

For such materials it is desirable for there to be a miscibility gap due to magnetism (Fig. 10.70(a, b)) as described in Chapter 8. In these circumstances, spinodal decomposition can occur by the formation of paramagnetic and ferromagnetic phases. The best magnetic properties can be produced if annealing is performed just below the temperature where instability begins.

Figure 10.71 shows a calculated isothermal section for Fe–Cr–Co at 1200 K, showing how the miscibility gap in the binary systems is expanded in the ternary. It should be noted that these sections are metastable, as the σ phase would precipitate out in equilibrium. However, if heat treatments are done for sufficiently short times, spinodal decomposition occurs without precipitation of σ. The effect of the expansion of the miscibility gap in the ternary means that higher heat-treatment temperatures can be used, allowing a material with a higher Curie temperature and subsequently higher saturation magnetisation to be produced. Heat treatments for these alloys can be sensitive to small changes in composition. Figure 10.72 shows a vertical section in Fe–Co–Cr at a ratio of $x_{Fe}/x_{Co} = 83/17$ and it can be seen that only a few at% differentiates alloys with a paramagnetic or a ferromagnetic matrix.

Al–Ni and Al–Ni–Co magnets work on identical principles to the Fe–Cr–Co magnets but, instead of considering a miscibility gap between paramagnetic and ferromagnetic phases which are disordered, the paramagnetic phase is, in this case, ordered. Figures 10.73(a, b) show an isothermal and a vertical section through the Fe–Ni–Al ternary system produced by a combination of experiment and calculation (Hao *et al.* 1984). Additions of Co were made to this basic system and, in accord with thermodynamic calculations (Nishizawa *et al.* 1983), both the peak temperature of the miscibility gap and the region of immiscibility in the quaternary are increased.

Good magnetic properties in these alloys are obtained under the following conditions: (1) The ferromagnetic α_1 phase is present as isolated particles embedded in a weakly magnetic or non-magnetic matrix of α_2; (2) the particles are uniaxially aligned; and (3) the volume fraction of α_1 is in the range 0.4–0.6

Unfortunately, Al–Ni and Al–Ni–Co magnets suffer from the disadvantage of being hard and brittle, leading to problems with machining which becomes expensive and difficult. Using a mainly experimental phase-diagram approach, Ishida *et al.* (1991) were able to design an alloy which contained a small amount of ductile f.c.c. γ phase distributed along the grain boundaries of the alloy. This

References are listed on pp. 402–408.

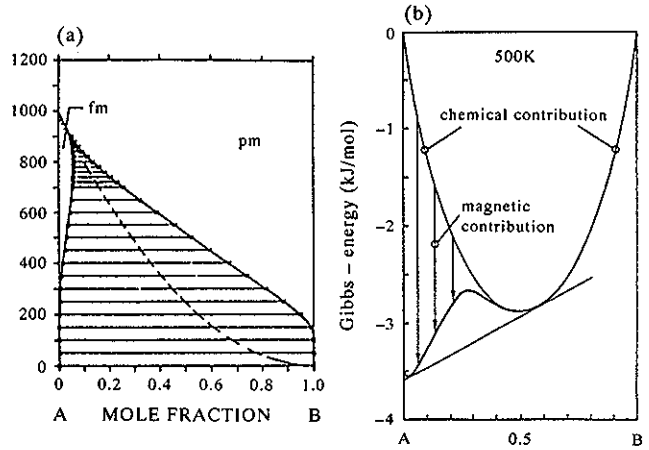

Figure 10.70 (a) Phase diagram for an A–B alloy system exhibiting phase separation due to magnetism and (b) underlying Gibbs energy vs composition curve showing the contribution from chemical and magnetic energies (from Inden 1987).

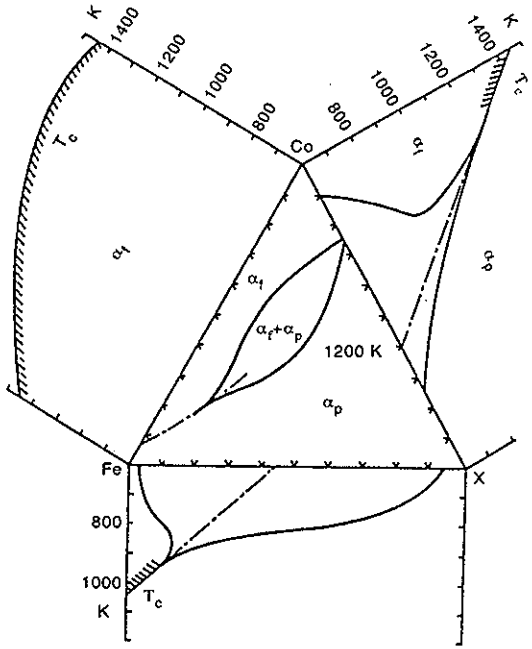

Figure 10.71 Calculated isothermal sections for Fe–Cr–Co at 1200 K (from Inden 1987, Nishizawa *et al.* 1979b).

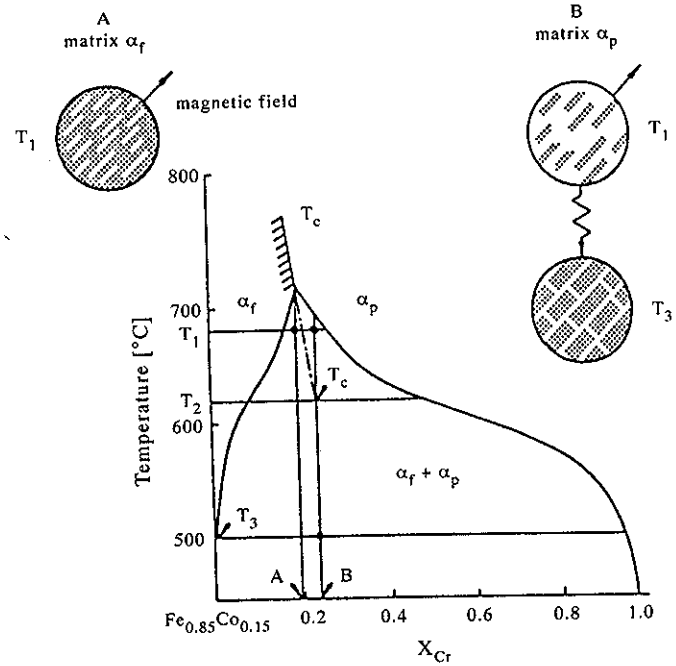

Figure 10.72 Calculated vertical section through the Fe–Cr–Co system at a constant ratio $x_{Fe}:x_{Co}$ of 83:17 (from Inden 1987, Homma *et al.* 1981). T_c is the Curie temperature.

microstructure significantly improves hot workability and leads to the possibility of producing ductile material.

10.6.5.2 Rapidly solidified in-situ metal matrix composites. A design project for alloys based on the Fe–Cr–Mo–Ni–B system, and produced by rapid solidification, was undertaken by Pan (1992). During processing a mixture of borides is formed inside a ductile Fe-based matrix which makes the alloys extremely hard with high moduli. These alloys provide a good example of how phase-diagram calculations were able to provide predictions which firstly helped to identify unexpected boride formation (Saunders *et al.* 1992) and were ultimately used in the optimisation of the modulus of a shaft material for gas turbines (Pan 1992).

The alloys are first produced by rapid solidification and are amorphous in nature. They are either directly fabricated as powders, by a process such as high-pressure gas atomisation (HPGA), or by melt-spinning of ribbons, which are subsequently pulverised to form a powder (<150 μm). The powders are then consolidated by hot extrusion between 950–1050°C where the initial amorphous structure breaks down and forms a fine dispersion of stable borides in a ductile Fe-based matrix.

References are listed on pp. 402–408.

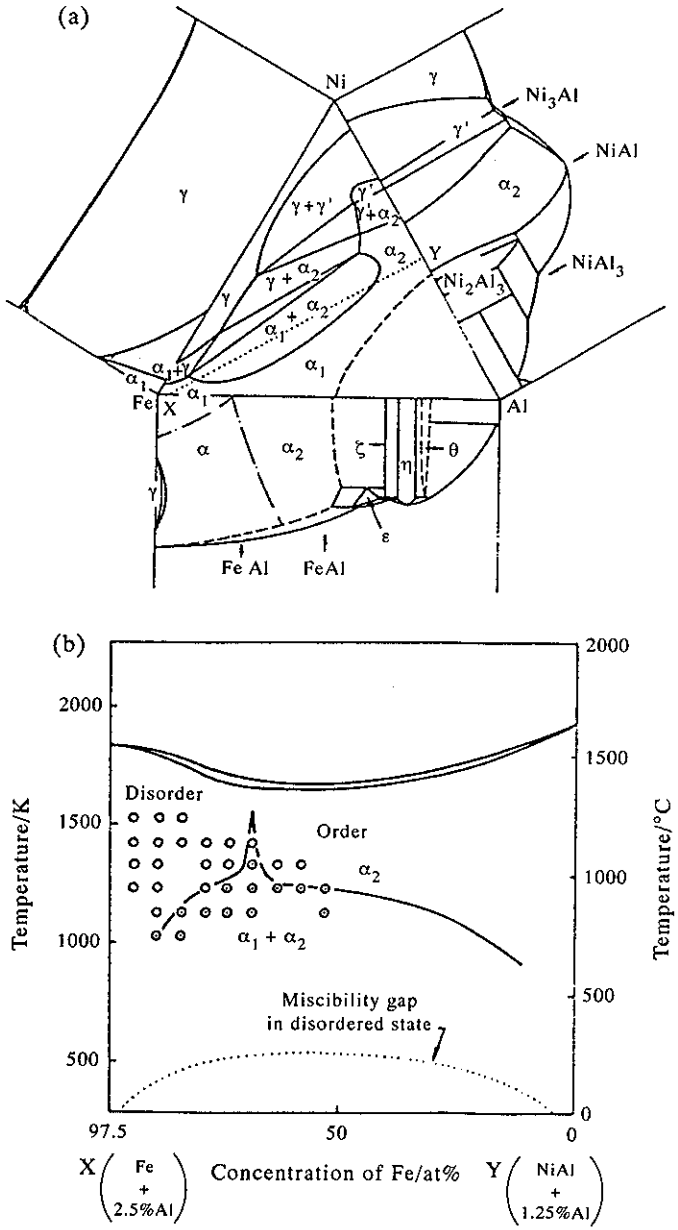

Figure 10.73 (a) Isothermal and (b) vertical sections from the Ni–Fe–Al phase diagram (Ishida and Nishizawa 1991).

Because of the inherently non-equilibrium nature of the production route, the first question which needed to be answered was whether the phases present in the alloy were in fact stable, so that equilibrium calculations could actually be used to design these alloys. To this end CALPHAD calculations were combined with a detailed experimental characterisation of a $Fe_{70}Cr_{18}Mo_2B_{10}$ alloy (Kim *et al.* 1990, Pan 1992). The TEM and XRD results confirmed earlier work (Xu *et al.* 1985) which stated that an orthorhombic boride M_2B was present and its composition was Cr-rich. However, they also showed that a proportion of the borides (~10%) were Mo-rich and that the Fe-based matrix was martensitic. The latter result was particularly surprising because of the high level (20at%) of α-ferrite stabilisers Cr and Mo. Furthermore, initial analysis of diffraction patterns from the TEM work indicated that the structure of the Mo-rich boride was a tetragonal type whose structure had not been reported in previous literature (Kim and Cantor 1988).

Calculated phase equilibria for this alloy produced the following predictions:

(1) The existence of a Cr-rich M_2B phase.
(2) There would be a substantial proportion (7.3%) of the U_3Si_2-type, M_3B_2 boride in the alloy with high levels of Mo.
(3) The Fe-based matrix would be austenitic at 1000°C but transform to ferrite below 857°C, thus giving a reason for the observed martensitic structure.

Based on the prediction for the M_3B_2 boride, and its observed lattice parameter variation with Fe, Cr and Mo levels, the structure of the Mo-rich phase was re-evaluated and clearly shown to be primitive tetragonal of the U_3Si_2-type (Kim *et al.* 1990). This work also gave results for ratio of Fe:Cr:Mo in the various phases which were in excellent agreement with those predicted at 1000°C.

It is clear that the input of the phase-diagram predictions greatly helped in understanding the evolution of microstructure in this alloy, and although the alloys were produced by a highly non-equilibrium route, the calculations also showed that the phases present after extrusion were the stable phases for the alloy, so design criteria based on equilibrium calculations could therefore be used. A further advantage of the calculation route was that the number of alloys which needed to be examined, in order to achieve the optimum microstructure/property combination for the design criteria of the turbine shaft, could be dramatically reduced (Pan 1992, Miodownik 1993).

In order to evaluate the role of the various phases, it was necessary to design distinct alloys where the matrix was either austenitic or ferritic. Figure 10.74 shows the principle by which this was achieved for Fe–Cr–B alloys where it can be seen that only a small change in Cr level puts an alloy into a region where it is fully ferritic at consolidation temperatures. Alloys from the Fe–Cr–Mo–B system were then designed so that the matrix was fully ferritic and a further set of alloys from the Fe–Cr–Ni–B system which were fully austenitic. Although producing stable microstructures, significant drops in strength and hardness were found in alloys

References are listed on pp. 402–408.

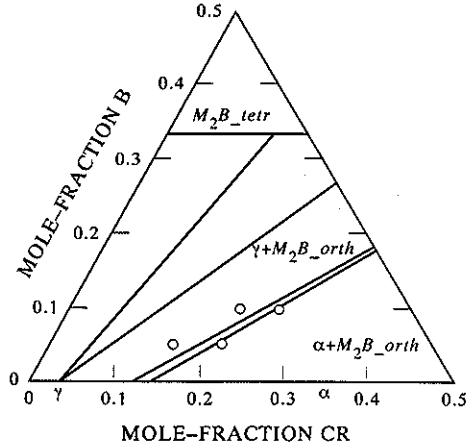

Figure 10.74 Calculated isothermal for Fe–Cr–B at 1000°C showing placement of high-B alloys which have either α or γ matrices at processing temperature (Pan 1992).

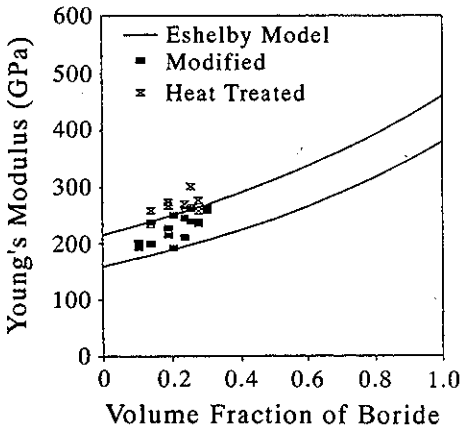

Figure 10.75 Comparison of calculated Eshelby curves for modulus with experimentally determined moduli for high-B ferrous base alloys (Pan 1992).

whose matrix was either fully ferritic or austenitic. It also became clear that small amounts of C were present in all alloys which was adding to the hardness of the martensite, hence enhancing its properties.

The next step was to optimise the ratio of M_3B_2 to MB_2 and various alloys were designed and tested to improve factors such as strength and modulus (Pan 1992). Eshelby analysis (Eshelby 1957, Withers *et al.* 1989) was used to predict modulus and good agreement was found with experimental measurement (Figure 10.75). It

was clear that modulus was significantly enhanced by increasing boride level but owing to morphological considerations (the borides were not aligned and had low aspect ratios) the modulus increase was less than was hoped for. In the end, alloys were designed to have martensitic matrices, approximately equal volumes of M_3B_2 and MB_2 and predicted modulii of between 245–255 GPa. All of these properties were achieved in the final experiments . One of the limiting factors in looking at higher amounts of M_3B_2, which were more finely dispersed and, hence, potentially gave greater strength, was that high liquidus temperatures made it difficult to melt such alloys.

10.6.5.3 The design of duplex stainless steels. Lee (1995) reported on work relating to the design of duplex stainless steels using a predominantly thermodynamic approach. Four important properties were chosen as being critical to performance, and these were: (1) strength, (2) toughness, (3) weldability and (4) corrosion resistance. Of these, strength was considered to be the least critical in the alloy design process, as this was heavily controlled by factors such as work hardening and grain size, and would be more effectively controlled by thermomechanical processing rather than design of composition. Lee (1995) then identified critical factors associated with phase equilibria which would affect the other three properties. These were the stability of austenite at high temperatures for weldability, sigma formation for toughness and the composition of austenite in local equilibrium with $M_{23}C_6$ for corrosion resistance. These factors could then be combined to give an overall performance criterion. The rationale for the choice of favourable thermodynamic properties was based on the following arguments.

Weldability. It had been previously reported (Norstrom *et al.* 1981) that an increase in austenite amount was beneficial to weldability. Further, Cao and Hertzman (1991) had reported that loss of impact toughness because of ferrite formation during welding could be recovered by re-formation of austenite at lower temperatures. Lee (1995) subsequently concluded that increased stability of austenite above the heat-treatment temperature would be beneficial to weldability. Therefore, the amount of austenite at 1350°C was taken as a criterion for alloy design, higher values being given a positive rating compared to lower values.

Sigma formation. While σ-phase formation is known to cause embrittlement in duplex stainless steels, Lee (1995) argued that the important factor in the process was the driving force for precipitation rather than the potential amount of σ which might be formed. This was because only small amounts are actually necessary to cause embrittlement (Norstrom *et al.* 1981) and, therefore, the early stage of precipitation should be considered more important than the final equilibrium state. While nucleation is a complex process, Lee (1995) suggested that, for the purpose of alloy design, nucleation parameters for σ such as interfacial energies, misfit strain energies, etc., would be approximately equal for alloys which lay close in composition to the original alloy. This would mean that the driving force for

References are listed on pp. 402–408.

Table 10.3. Composition of candidate alloys and results of calculations on toughness, weldability and corrosion resistance. Calculation was conducted assuming an annealing temperature of 1050°C, 0.8%Mn, 0.7%Si and 0.024%C (wt%). PRE value in the heading of the table indicates value for SAF2205 (from Lee 1995)

Alloy composition (wt%)				Toughness	Weldability	Corrosion resistance	
N	Ni	Mo	Cr	ΔG for σ	High temp. austenite %	Cr content in austenite	PRE (37.28)
0.14	7.5	0	27.15	X	—	—	
0.14	7.5	1	26.21	X	—	—	
0.14	7.5	2	25.27	X	—	—	
0.14	7.5	3	24.33	X	—	—	
0.14	7.5	4	23.40	X	—	—	
0.14	6.5	0	25.93	X	—	—	
0.14	6.5	1	24.95	X	—	—	
0.14	6.5	2	23.97	X	—	—	
0.14	6.5	3	22.99	X	—	—	
0.14	6.5	4	22.01	√	√ (3.2)	X	41.55
0.14	5.5	0	24.69	X	—	—	
0.14	5.5	1	23.67	√	X (0.3)	√	32.80
0.14	5.5	2	22.64	√	X (0.8)	√	35.08
0.14	5.5	3	21.62	√	X (1.4)	X	37.36
0.14	5.5	4	20.60	√	X (1.9)	X	39.63
0.14	4.5	0	23.43	√	XXX (0.0)	√√√	28.76
0.14	4.5	1	22.37	√	XX (0.0)	√√	31.00
0.14	4.5	2	21.29	√	X (0.0)	√	33.23
0.14	4.5	3	20.21	√√	X (0.2)	√	35.45
0.14	4.5	4	19.13	√√√	X (1.0)	X	37.67
0.20	7.5	0	28.47	X	—	—	
0.20	7.5	1	27.54	X	—	—	
0.20	7.5	2	26.61	X	—	—	
0.20	7.5	3	25.69	X	—	—	
0.20	7.5	4	24.77	X	—	—	
0.20	6.5	0	27.24	X	—	—	
0.20	6.5	1	26.27	X	—	—	
0.20	6.5	2	25.31	X	—	—	
0.20	6.5	3	24.34	X	—	—	
0.20	6.5	4	23.38	X	—	—	
0.20	5.5	0	25.99	X	—	—	
0.20	5.5	1	24.99	X	—	—	
0.20	5.5	2	23.98	√	√ (6.5)	√	38.22
0.20	5.5	3	22.97	√	√√ (7.2)	√	40.51
0.20	5.5	4	21.97	√	√√√ (7.8)	√	42.80
0.20	4.5	0	24.73	√	√ (3.6)	√√√	31.87
0.20	4.5	1	23.68	√	√ (4.6)	√√	34.12
0.20	4.5	2	22.63	√	√ (5.4)	√	36.37
0.20	4.5	3	21.57	√	√ (6.3)	√	38.61
0.20	4.5	4	20.51	√√	√√ (7.0)	√	40.85

nucleation would effectively be the dominating criteria for the initial precipitation.

Corrosion resistance. The main criterion here was judged to be the level of Cr in the matrix phase and the avoidance of Cr depletion in the austenite which would be controlled by the precipitation of $M_{23}C_6$ in the early stages. A criterion was therefore placed on alloy design where high levels of Cr in the austenite phase in 'local equilibrium' with $M_{23}C_6$ would be given a positive rating.

It is also desirable for the alloy to have as high a Pitting Resistance Equivalent (PRE) value as possible and Lee (1995) calculated this number using the formula

$$\text{PRE} = \text{wt\%Cr} + 3.3\text{wt\%Mo} + 30\text{wt\%N} + 0.5\text{wtNi} - 0.5\text{wt\%Mn} - 30\text{wt\%C}.$$

Lee (1995) then constructed a matrix of 40 candidate alloys, close to the SAF2205 composition of Fe–22Cr–5.5Ni–3Mo–1.7Mn–0.4Si–0.14N–0.025C (in wt%) which are given in Table 10.3. Calculations were then made to establish the magnitude of the various criteria described previously and a tick ($\surd$) is shown where improvement was predicted over SAF2205, (**X**) where there would be a deterioration in the property and (—) denotes that this property was not calculated. On the basis of this approach it is clear that five alloys with high N would give an improvement in all three criteria and also give a higher PRE number.

10.6.5.4 Design of high-strength Co–Ni steels. Grujicic *et al.* (1987) and Grujicic (1991) have developed a procedure to design ultra-high-strength alloys based on M_2C-hardened Co–Ni steels. They set a design criterion for producing an alloy with good fracture toughness (K_{IC}~70–130 MPa$\sqrt{\text{m}}$) and an ultimate tensile strength (UTS) level between 2100 and 2400 MPa. They began with a commercial alloy AF1410 which, although falling far short of their ultimate goal, served as a starting point for their design programme. The composition of AF1410 is Fe–14Co–10Ni–2Cr–1Mo–0.15C (in wt%). It is primarily strengthened by M_2C, where M=Cr and Mo, and peak hardness is found on tempering at 510°C for 5 hrs.

Their initial aims were to assess the role played by Co on the carbide phases and to optimise the Cr, Mo and W levels subject to the requirements of a balanced composition where $x_{Mo} + x_{Cr} + x_W = 2x_C$. Further, constraints were to limit the C level at 0.25wt% and the nickel level at 10wt%.

The first part of the work was to calculate the driving force for the precipitation of M_2C from their alloys, as this is the factor which would govern its precipitation behaviour in the initial stages. They did this for an alloy with the fixed-base composition Fe–14Co–10Ni–0.25C, at the proposed heat-treatment temperature of 783 K, and varied the W, Mo and Cr levels using the formula given in the previous paragraph. Results were plotted in a ternary format (Fig. 10.76(a)) and show how the greatest driving force is found for Mo-rich alloys with the relative effect of various elements on ΔG being in the order Mo>Cr>W. As carbides other than M_2C would also form in their alloys, they plotted driving forces to form $M_{23}C_6$ and M_6C,

References are listed on pp. 402–408.

which are shown in Figs. 10.76(b, c). It can be seen that the lowest driving forces to form these carbides were in Mo-rich alloys and, hence, such alloys would maximise the yield of M_2C.

Grujicic (1991) then made a series of calculations to estimate the M_2C coarsening rate in these types of alloys. This is important because metastable cementite is often a predecessor precipitate to M_2C and deleterious to mechanical properties. The cementite can be removed by prolonging the tempering treatment, but this causes subsequent coarsening of the desirable M_2C. Using simple coarsening theory, they were able to determine that W-rich alloys would have the greatest resistance to

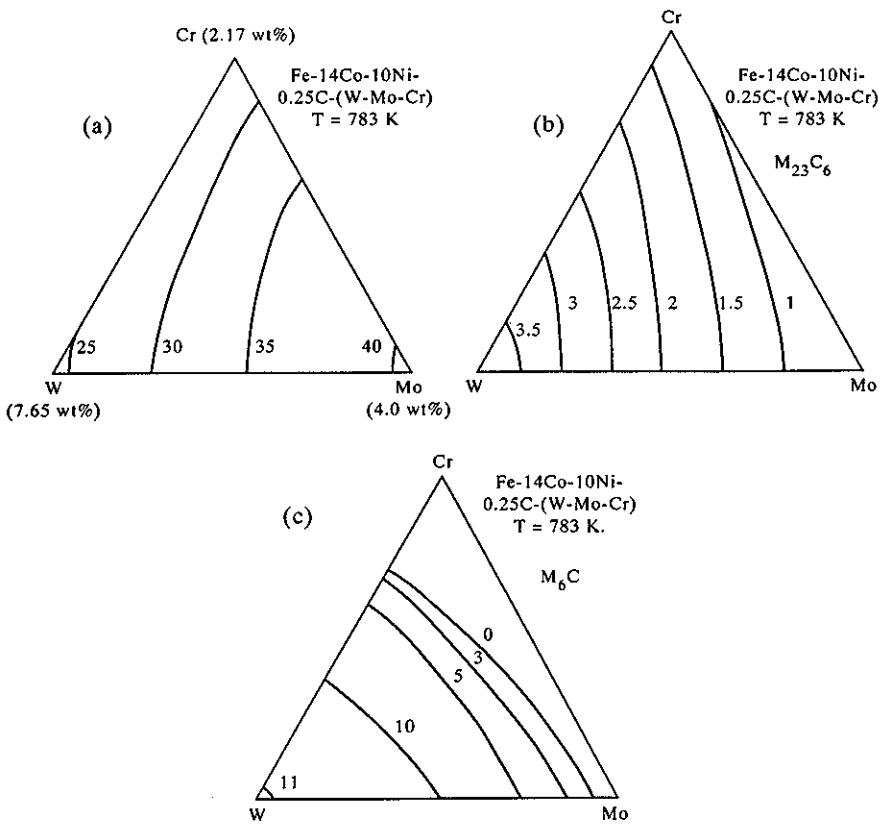

Figure 10.76 Variation of the driving force (kJ mol^{-1}) for precipitation of (a) M_2C, (b) $M_{23}C_6$ and (c) M_6C from ferrite at 783 K in a Fe–14Co–10Ni–0.25C–(W–Mo–Cr) alloys with balanced alloy additions of Mo, Cr and W (Grujicic *et al.* 1987).

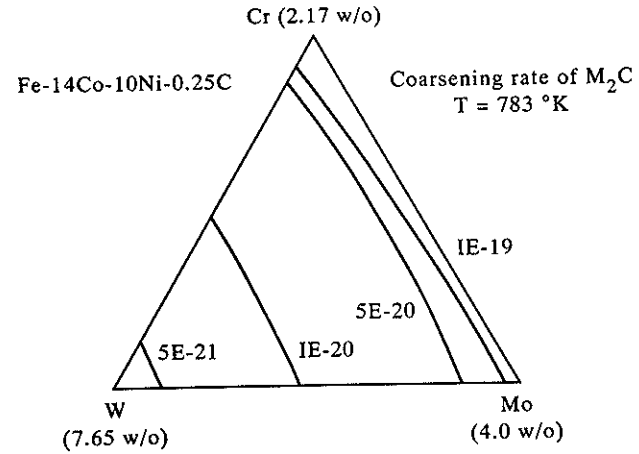

Figure 10.77 Coarsening rate of M_2C at 783 K in a Fe–14Co–10Ni–0.25C–(W–Mo–Cr) alloys with balanced alloy additions of Mo, Cr and W (Grujicic 1991).

coarsening; their calculated results are shown in Fig. 10.77, again using ternary axes. The design of the alloy now becomes a subtle balance of increasing W levels to enhance the coarsening resistance of M_2C, but keeping Cr and Mo levels sufficiently high to minimise the potential for precipitation of the other carbides, $M_{23}C_6$ and M_6C.

The general design process for these alloys was extended by Grujicic and Olson (1988) to consider how ferrite/M_2C equilibria could be adjusted by considering coherency strains at the matrix/carbide interface during the early stages of precipitation. Their calculations indicated that Fe would substitute for Cr in the case of coherent equilibrium and that the C stoichiometry would be shifted significantly from an ideal M_2C ratio. This affects coarsening resistance as well as driving force for precipitation.

In a further aspect of the design, compositions were adjusted to maximise the fracture toughness of the alloy by maximising its transformation toughening behaviour (Haidemenopoulos *et al.* 1989). This toughening occurs because of deformation-induced martensite which forms at the crack tip as it moves through the dispersion of austenite which is retained in the alloy. The design criteria used here were that there should be both as large a volume change on transformation to martensite as possible and also that the driving force to form martensite should be as high as possible in the retained austenite. Magnetic Gibbs energy contributions, as well as those due to composition, were taken into account and it was concluded that deformation-induced transformation toughness would be maximised by moving from the 'ideal' AF1410 composition to an alloy with significantly higher levels of Ni.

References are listed on pp. 402–408.

10.6.6 Slag and slag–metal equilibria

10.6.6.1 Matte–slag–gas reactions in Cu–Fe–Ni sulphide ores. Sulphide ores are a major source of Cu, Ni and precious metals. A basic principle of the extraction processes is to blow air into the molten sulphide in order to oxidise (1) S, which forms a gas and (2) Fe, which forms predominantly FeO and then partitions to a slag phase which covers the matte. A key element in the recovery of the metals is the solidification of the matte which separates into a sulphur-rich matte and metal-rich liquid. This process may occur under non-equilibrium conditions with precious metals concentrating in the last metallic liquid.

To obtain a better understanding of the process, calculations were performed by Dinsdale *et al.* (1988) and Taylor and Dinsdale (1990) for a pre-fused matte of Ni_3S_2, Cu_2S and FeS, heated to around 1270°C with an equivalent amount of oxide slag, and with O being blown into the matte. Calculations from the model system Cu–Fe–Ni–S–O are presented in Fig. 10.78 which shows the comparison between calculated and experimental values of the Fe/S partitioning in the matte as a function of SO_2 levels.

Calculations were then made for the amount of Cu and Ni levels in the slag as a function both of Fe in the matte and SO_2 levels. This showed that partitioning was

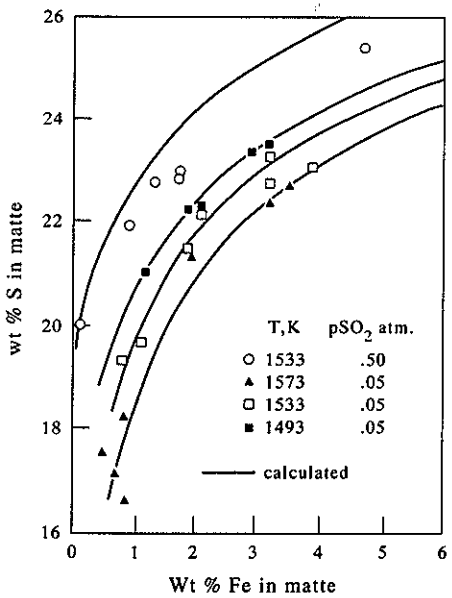

Figure 10.78 Comparison between calculated and experimental matte compositions (Ni:Cu wt ratio 2:1) at different temperatures and SO_2 partial pressures (from Taylor and Dinsdale 1990).

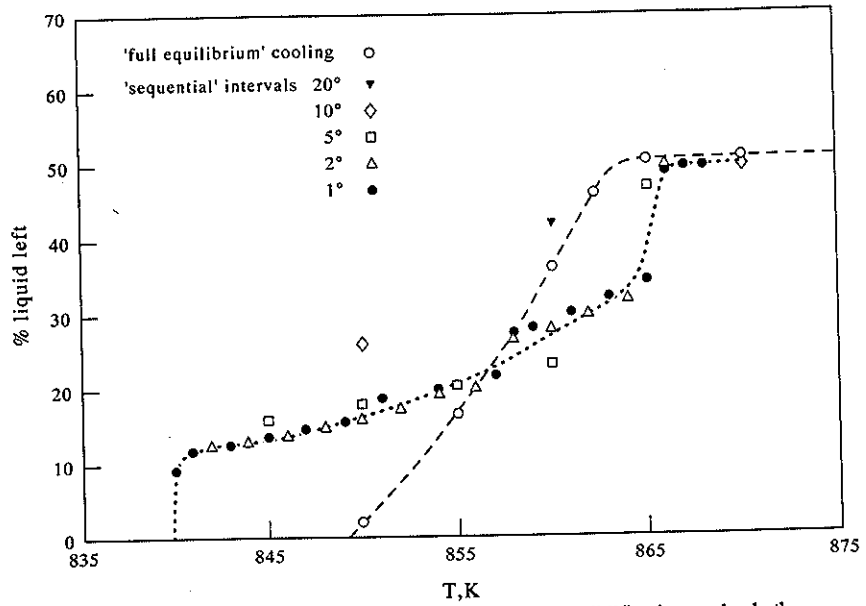

Figure 10.79 Percent liquid remaining during matte solidification under both equilibrium and 'Scheil–Gulliver' solidification conditions (from Taylor and Dinsdale 1990).

insensitive to SO_2 levels and it was only necessary to maintain significant levels of Fe in the matte to ensure that Cu and Ni uptake in the slag was minimised. The solidification of the matte was then modelled both when solidification occurred by an equilibrium process and alternatively in a non-equilibrium fashion, diffusion in the solid being considered negligible (the so-called 'Scheil–Gulliver' conditions, see Chapter 11). Figure 10.79 shows the calculated results and it is evident that the liquid is retained to lower temperatures than would occur by equilibrium freezing, and the model for non-equilibrium solidification predicted the formation of a new phase, which was consistent with experimental information.

10.6.6.2 Calculation of sulphide capacities of multi-component slags. The thermo-dynamics and kinetics of desulphurisation are of great importance to iron and steel making and the ability to predict the behaviour of sulphur associated with multi-component slags is, therefore, very desirable. To this end Pelton *et al.* (1993) recently described an approach to predict the sulphide-removing capacity in multi-component oxide slags. While a comprehensive database for oxides was already available, the inclusion of S had not yet been undertaken. Therefore it was not possible to calculate the necessary S activity and solubility directly through a

References are listed on pp. 402–408.

CALPHAD calculation. To overcome this difficulty they combined a semi-empirical model from Reddy and Blander (1987, 1989) with an equilibrium CALPHAD calculation for the multi-component oxide system SiO_2–Al_2O_3–TiO_2–CaO–MgO–MnO–FeO. The approach can be summarised as follows.

The exchange of O and S between an oxide slag and other phases can be written in general terms as

$$A_nO_{(\text{liq})} + \tfrac{1}{2}S_{2\,(\text{gas})} = A_nS_{(\text{liq})} + \tfrac{1}{2}O_{2\,(\text{gas})} \tag{10.2}$$

where A_nO and A_nS are components of a slag, with A being a particular cation. An equilibrium constant can be defined for this reaction as

$$K_A = \frac{a_{A_nS}}{a_{A_nO}}\left(\frac{P_{O_2}}{P_{S_2}}\right)^{1/2} = \exp\left(\frac{-G^\circ_A}{RT}\right) \tag{10.3}$$

where a_{A_nO} and a_{A_nS} are the activities in the slag and G°_A is the standard Gibbs energy of reaction. As the amount of S in solution is small, it was assumed that Henry's law could be applied such that a_{A_nS} varies directly as the amount of dissolved S. Further, it was assumed that for a given oxide slag composition, a_{A_nO} would be nearly equal to its value in the sulphur- free slag. From this the sulphide capacity of a slag (C_S) can be derived (Fincham and Richardson 1964) as

$$C_S = (\text{wt\%S})\left(\frac{P_{O_2}}{P_{S_2}}\right)^{1/2} \tag{10.4}$$

where (wt%S) is the amount of dissolved sulphur. The sulphide capacity for any given slag will be constant as long as the dissolved S is relatively low and, therefore, the higher the sulphide capacity, the higher the S content of the slag.

Equation (10.4) relies on a knowledge of both the sulphide and oxide activities. However, S was not yet included in their database for oxides. They therefore utilised the approach of Reddy and Blander (1987, 1989) to relate a_{A_nS} to the S content and sulphide capacities could then be predicted through calculation of a_{A_nO} alone. The approach yields the following expressions for sulphide capacities for basic and acid slags:

Basic slags $x_{SiO_2} \le 1/3$

$$\left(\frac{C_S}{C^\circ_S}\right) = a_{A_nO}\frac{(1-2x_{SiO_2})}{(x_{A_nO}M_{A_nO} + x_{SiO_2}M_{SiO_2})} \tag{10.5}$$

Acid slags $x_{SiO_2} \ge 1/3$

$$\left(\frac{C_S}{C^\circ_S}\right) = a_{A_nO}\frac{x_{SiO_2}}{(x_{A_nO}M_{A_nO} + x_{SiO_2}M_{SiO_2})}\cdot\left(\frac{1-x_{SiO_2}}{2x_{SiO_2}}\right)^2 \tag{10.6}$$

and

$$C_S^\circ = \frac{1000\, M_S K_A}{\gamma^\circ_{A_nS}} \tag{10.7}$$

where x and M denote, respectively, the moles and molecular weights of the various components. The Henrian activity coefficient of A_nS, $\gamma^\circ_{A_nS}$, is then assumed to be equal to 1, and if K_A for each component is known, the sulphide capacity can be calculated for each oxide component. Values of K_A were obtained from assessed thermodynamic values. The various values of C_S for each oxide component were then obtained from the following equation:

$$\log C_S = y_A \log C_{S(A)} + y_B \log C_{S(B)} + y_C \log C_{S(C)} + \cdots \tag{10.8}$$

where $\log C_{A(S)}$ is the value of $\log C_S$ in the binary A_nO–SiO_2 at the same value of x_{SiO_2} as in the multi-component system and

$$y_A = \frac{x_{A_nO}}{(x_{A_nO} + x_{B_nO} + x_{C_nO} + \cdots)}. \tag{10.9}$$

The approach yielded excellent results and Figs 10.80–10.83 show comparison of calculated and experimentally determined sulphide capacities in various multi-component slags.

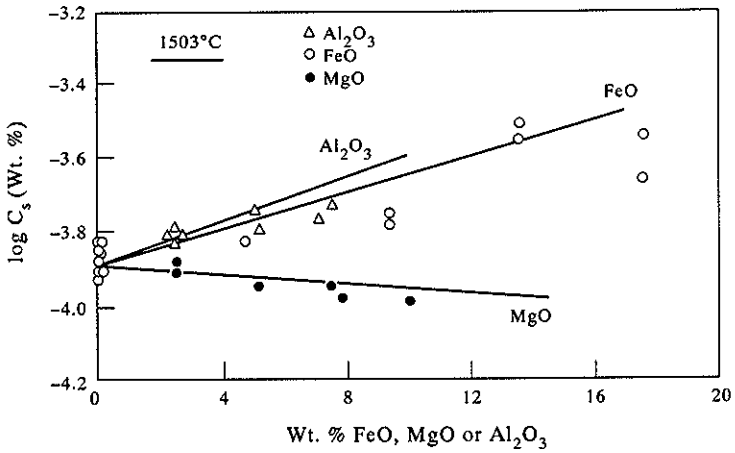

Figure 10.80 Comparison between calculated and experimental (Bronson and St-Pierre 1981) effects of Al_2O_3, FeO and MgO additions upon sulphide capacities of CaO–SiO_2 slags at a constant (CaO+AO)/(SiO_2+Al_2O_3) ratio, where A = Fe or Mg.

References are listed on pp. 402–408.

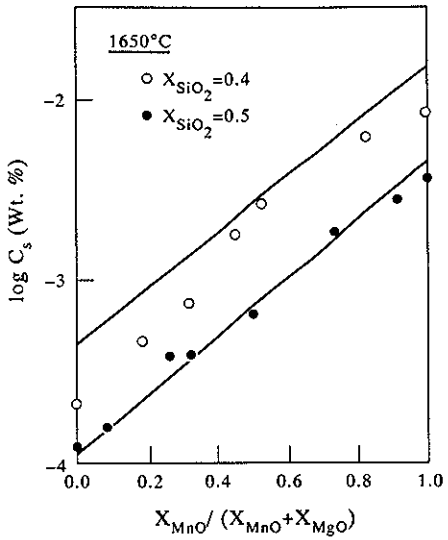

Figure 10.81 Comparison between calculated and experimental (Sharma and Richardson 1965) sulphide capacities at constant SiO_2 fraction in MnO–MgO–SiO_2 slags.

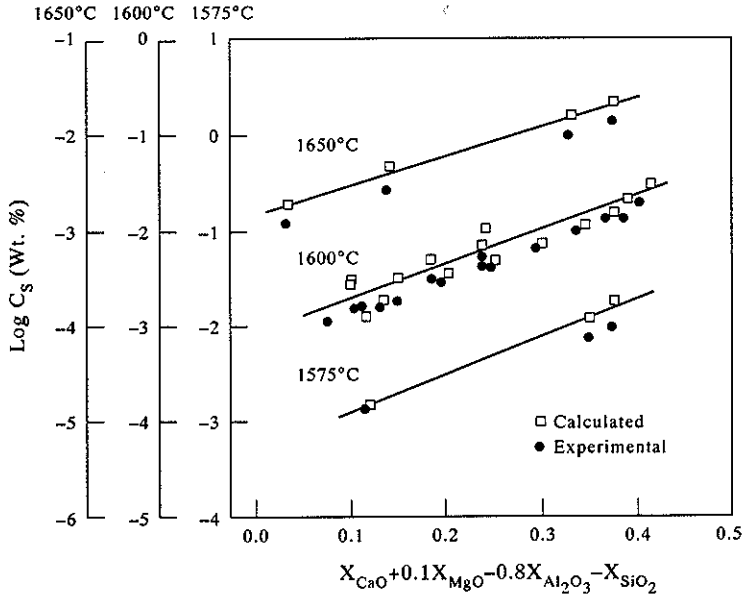

Figure 10.82 Comparison between calculated and experimental (Bronson and St-Pierre 1981) sulphide capacities in SiO_2–Al_2O_3–MgO–CaO–FeO slags.

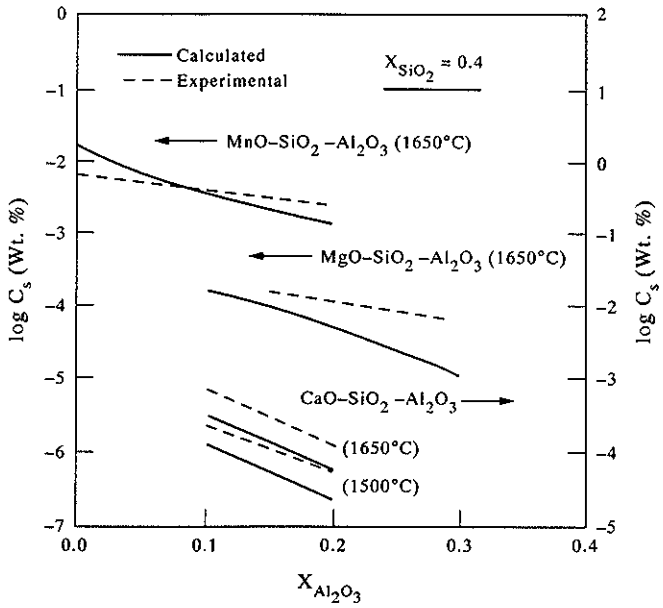

Figure 10.83 Comparison between calculated and experimental (Fincham and Richardson 1954, 1964, Sharma and Richardson 1965) sulphide capacities in $AO–SiO_2–Al_2O_3$ slags (where A = Mn, Mg, Ca) at a constant SiO_2 fraction of 0.4.

10.6.6.3 Estimation of liquidus and solidus temperatures of oxide inclusions in steels. The deformation of inclusions in steels has significant consequences on the hot workability of steels as well as for the mechanical properties of the final product. In order to increase their deformability there are at least three strategies (Matsumiya *et al.* 1987): (1), Reduction of their melting point; (2), deceleration of crystallisation; and (3), reducing their flow stress. If the melting point can be reduced sufficiently so that some liquid is present at the hot-working temperature, the inclusions would be expected to deform easily.

To this end, Matsumiya *et al.* (1987) made calculations for inclusions from the quinary system $SiO_2–Al_2O_3–CaO–MgO–MnO$, based on assessments of the component binary and ternary sub-systems. Figures 10.84(a, b) show two of the calculated ternary diagrams and Table 10.4 shows comparisons between calculated and experimentally determined liquidus temperatures for five oxide inclusions.

Figures 10.85(a, b) show phase fraction plots for inclusions 1 and 2 in Table 10.4. These are plotted in such a way as to show the cumulative amount of all phases as well as their individual amounts. A quasi-ternary diagram was then plotted for an 'ideal' inclusion with a fixed level of $Al_2O_3 = 20.4$wt% and MgO = 8.2wt% (Fig. 10.86). From this it can be seen that a slight increase in SiO_2 reduces the liquidus

References are listed on pp. 402–408.

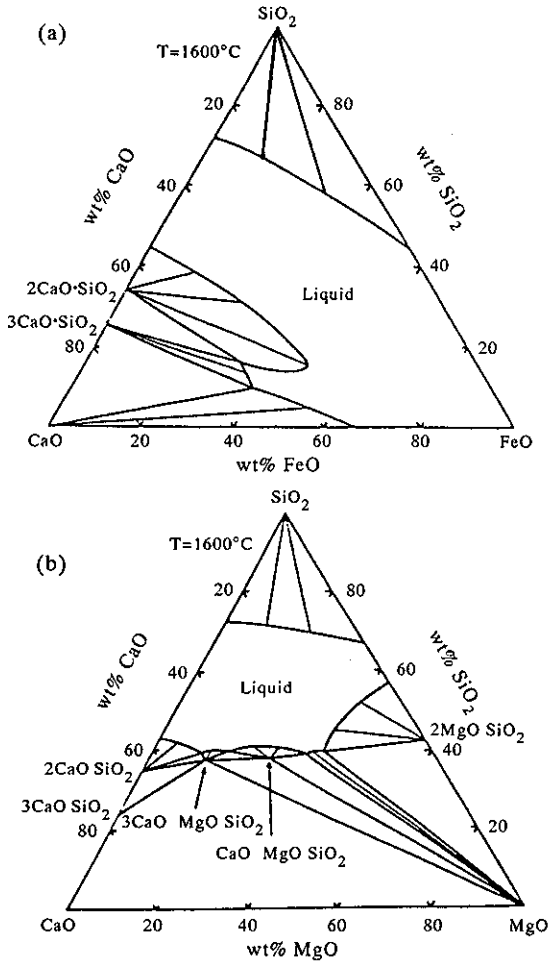

Figure 10.84 Calculated isothermal sections at 1600°C for (a) $CaO–FeO–SiO_2$ and (b) $CaO–MgO–SiO_2$ (Matsumiya *et al.* 1987).

temperature of inclusion 1 from Table 10.4. Taking this into account in a new 'ideal' inclusion, they made further calculations by varying the various levels of the component oxides with fixed SiO_2 content. From these calculations they were able to conclude that the liquidus temperature was sensitive to changes in the component oxides with sensitivity factors in the following order: $MnO > Al_2O_3 > MgO > CaO$. To realise the potential reductions in liquidus temperature of the inclusions, changes would be needed during the steelmaking process in the de-oxidiser, refining slags and refractory materials.

Table 10.4. Compositions, liquidus temperatures and primary phases of oxide inclusions

No.	Oxide composition (weight fractions)					Liquidus (°C)		Primary phase
	SiO_2	Al_2O_3	CaO	MgO	MnO	Calc.	Exp.	
1	0.459	0.204	0.153	0.082	0.102	1290	1300	$MgO.Al_2O_3$
2	0.500	0.050	0.020	0.230	0.200	1390	1404	$2MgO.SiO_2$
3	0.4208	0.2956	0.2108	0.0441	0.0287	1450	1460	$CaO.2SiO_2.Al_2O_3$
4	0.5081	0.3559	0.0833	0.0437	0.0090	1550	>1500	$CaO.2SiO_2.3Al_2O_3$
5	0.7749	0.1830	0.0012	0.0054	0.0355	1280	>1650	$2SiO_2.3Al_2O_3$
6	0.5647	0.2712	0.0270	0.0010	0.1361	1470	>1500	$2SiO_2.3Al_2O_3$

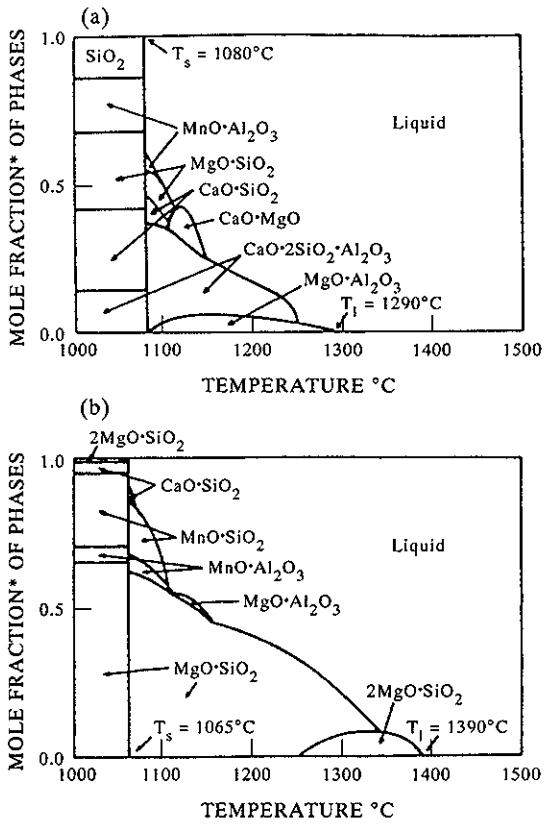

Figure 10.85 Calculated phase fraction vs temperature plots for oxide inclusions nos (a) 1, (b) 2 and (c) 3 from Table 10.4.

References are listed on pp. 402–408.

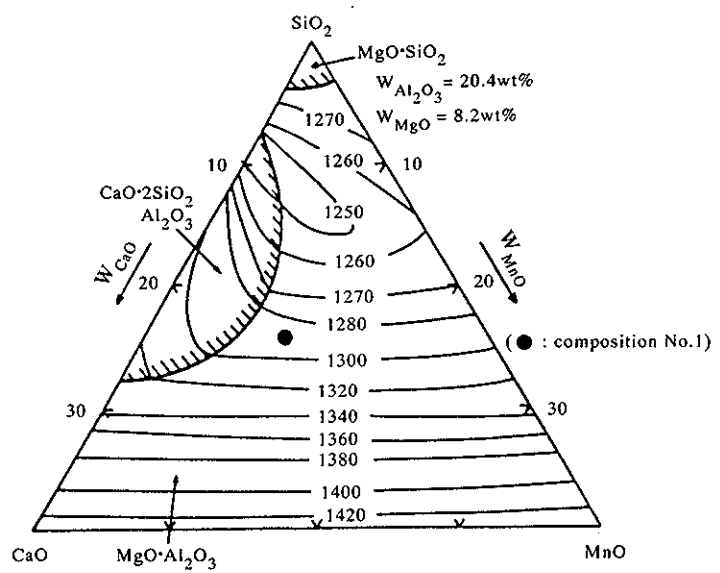

Figure 10.86 Calculated liquidus surface of the five-component oxide system with fixed values of 20.4wt%Al_2O_3 and 8.2 wt%MgO.

10.6.7 Complex chemical equilibria

10.6.7.1 CVD processing. CVD (chemical vapour deposition) processing is an area where calculations using mainly a substance database have proved valuable in understanding the process conditions for deposition of silicides, borides, carbides, etc. A good example of such calculations is provided by Vahlas *et al.* (1996) who looked at the deposition of WSi_2 from various gaseous environments. They utilised a substance database for the elements Si–W–Cl–H–O–Ar where 46 species in the gas phase and 20 stoichiometric condensed phases were considered in the calculation.

They first calculated a so-called 'CVD diagram' for the system WF_6–SiH_4–H_2–Ar, representing the incoming gas, which shows the phases which will be deposited as a function of partial pressure of WF_6 and SiH_4 (Fig. 10.87). The lines separating the various deposition regimes have 'bands of uncertainty' superimposed to reflect the uncertainty arising from the assessment of the thermodynamic data for the total system. It is clearly seen that the deposition of *pure* WSi_2 will be difficult using these input gases. In order to find a less sensitive system the case of WCl_4–SiH_4–H_2–Ar was considered, whose CVD diagram is shown in Fig. 10.88. It can now be seen that the single-phase region for WSi_2 has significantly expanded which means that the CVD process will be less sensitive to composition fluctuations in the input gas

itself, or fluctuations in the gas due to transport phenomena within the CVD deposition chamber. Further variations occur when SiH_4 is substituted for by $SiCl_2H_2$ and the width of the WSi_2 single-phase region expands even further (Fig. 10.89), providing even less demanding conditions for the deposition of pure WSi_2.

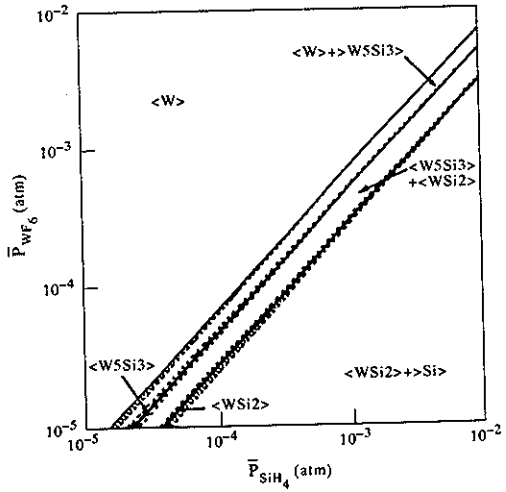

Figure 10.87 Calculated CVD phase diagram for the WF_6–SiH_4–H_2–Ar system at $T=1000$ K, $P_{total}=1$ atm and $P_{ar}=0.9$ atm (from Vahlas *et al.* 1996).

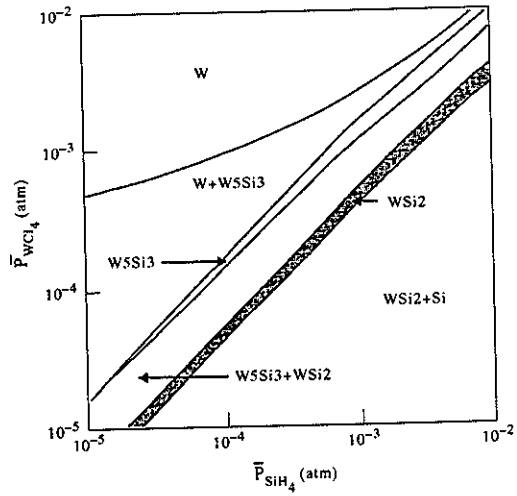

Figure 10.88 Calculated CVD phase diagram for the WCl_2–SiH_4–H_2–Ar system at $T=1000$ K, $P_{total}=1$ atm and $P_{ar}=0.9$ atm (from Vahlas *et al.* 1996).

References are listed on pp. 402–408.

The substitution of $TiCl_4$ for WCl_4 yields the CVD diagram as shown in Fig. 10.90 (Vahlas *et al.* 1996) and it can clearly be seen that the CVD diagram is totally different, demonstrating both the system specific nature of such diagrams and the importance of the underlying thermodynamics in determining how the process will occur in practice.

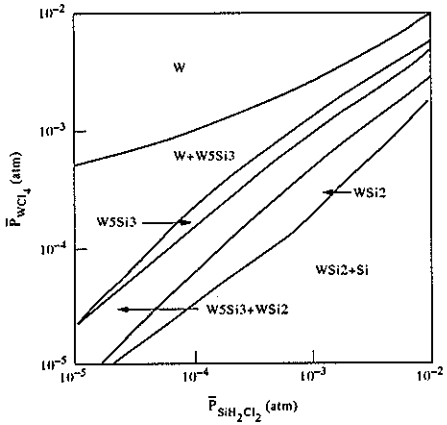

Figure 10.89 Calculated CVD phase diagram for the WCl_4–$SiCl_2H_2$–H_2–Ar system at $T=1000$ K, $P_{total}=1$ atm and $P_{ar}=0.9$ atm (from Vahlas *et al.* 1996).

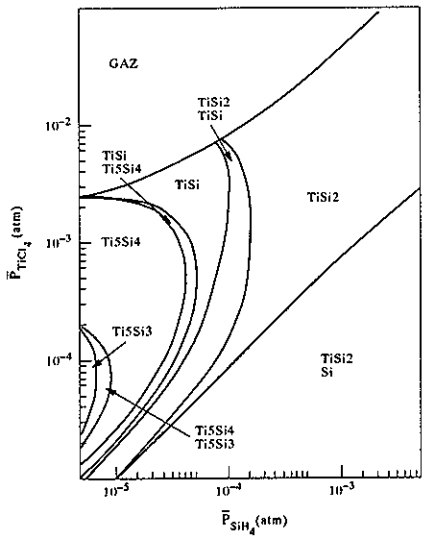

Figure 10.90 Calculated CVD phase diagram for the $TiCl_4$–SiH_4–H_2–Ar system at $T=1000$ K, $P_{total}=1$ atm and $P_{ar}=0.9$ atm (from Vahlas *et al.* 1996).

10.6.7.2 Hot-salt corrosion in gas turbines. In a wide variety of cases, Ni-based super-alloys are protected from corrosive attack in gas turbine engines by the formation of a surface layer of Cr_2O_3. However, in marine environments, NaCl can become concentrated in the incoming gas and lead to reaction with sulphur-containing combustion products to form Na_2SO_4. This then condenses onto the Cr_2O_3 layer which leads to the dissolution of Cr_2O_3, exposing the alloy itself to corrosive attack from the atmosphere, which is both oxidising and sulphidising. This type of attack is often called 'hot-salt corrosion' and Barry and Dinsdale (1996) examined this process using a substance database as the basis for their calculations.

The required data is for the gas and solid phases in the system NaCl–NaOH–Na_2CrO_4–Na_2SO_4. Some solubility was allowed for in the condensed solid phases, mainly in terms of binary interactions between the respective components which form simple phase diagrams (see for example Fig. 10.91). Calculations were then made relating to a gas turbine operating at a fuel/air ratio of 50:1, at 15 bar and 750°C. The fuel was taken to have a composition approximating to the formula $CH_{1.8}$. On the basis of these assumptions, the combustion products were calculated to be predominantly N_2, O_2, CO_2 and H_2O, their respective partial pressures being, 11.6, 2.216, 0.61 and 0.55 bars. 1% sulphur in the fuel would then cause the sum of the pressures of SO_2 and SO_3 to be 0.0026 bar. If only 1 ppm of NaCl were present this would cause the partial pressure of HCl in the gas to be 0.0046 bar, the residual sodium forming mainly as Na_2SO_4 on any exposed surfaces.

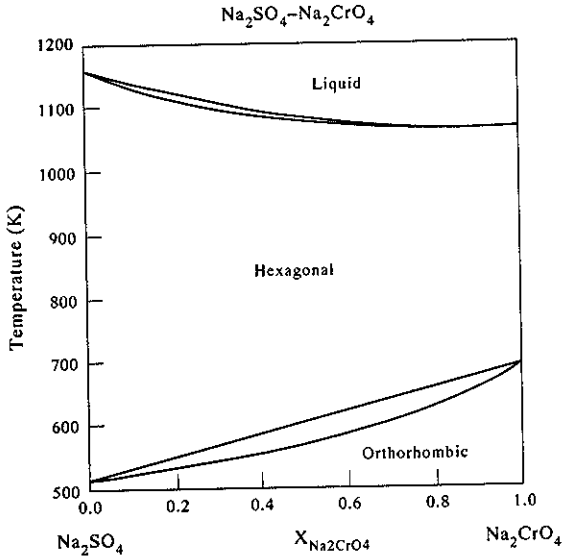

Figure 10.91 Calculated phase diagram for the Na_2SO_4–Na_2CrO_4 binary system (Barry and Dinsdale 1996).

References are listed on pp. 402–408.

10.6.7.3 Production of silicon in an electric arc furnace. Although not particularly complex in terms of chemical equilibrium, the production of Si in an electric arc furnace is a neat example of how equilibrium calculations can be made which take into account material flow during a dynamic process (Eriksson and Hack 1990). In practice, the furnace works continuously, with raw starting material supplied at the top of the furnace while gases circulate in such a way that there is a flow upwards with a counter-current flow of solid material which falls downwards. In order to simulate the reactions taking place in the furnace, it is necessary to take into account the fact that substances move in a temperature gradient during the process and that the temperature is controlled as much by the heat exchange and enthalpy of reactions as by external heating.

Eriksson and Hack (1990) developed a module for the ChemSage software code which would help examine cases where there is material and heat flow as well as chemical reactions. This is achieved by conceptually separating up the furnace into a number of separate parts or 'stages' where local chemical equilibrium can be assumed. Flow is then modelled by including distribution coefficients between the stages. So, for example, in a reactor with two stages, material which reacts in one stage can move to another stage, dependent on the flow direction. The accuracy of the programme in dealing with dynamic flow, which is non-equilibrium in nature, lies in how many stages are used. The use of many stages will allow smooth changes to be considered but will cause a substantial increase in computational time. For the Si arc furnace four stages were considered and these are shown schematically below.

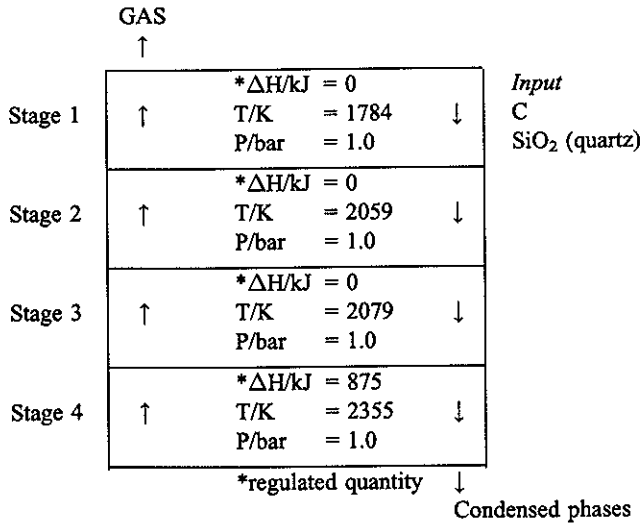

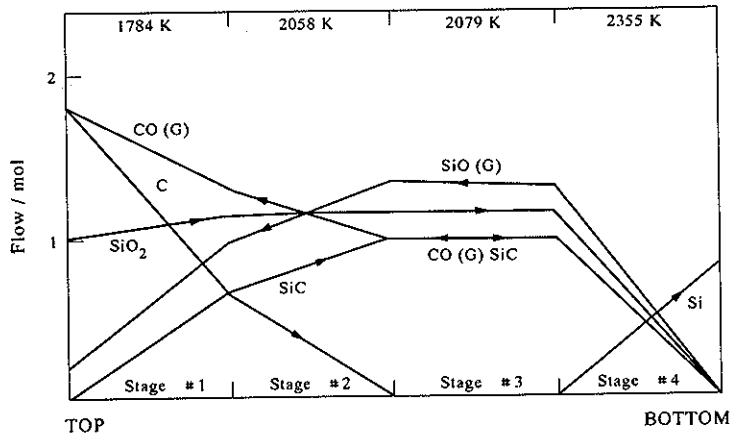

Figure 10.92 Flow scheme for various phases in a Si electric arc furnace (from Eriksson and Hack 1990).

The raw materials, 1 mole of SiO_2 and 1.8 moles of C are introduced into the top stage where the temperature is 1784 K, while the energy from the arc, 875 kJ per mole of SiO_2, was taken to be released only in the bottom stage of the reactor. The reactor assumes each stage has fixed temperature and therefore the enthalpy input to the other three stages arises solely from heat exchange and reaction. The flow scheme (Fig. 10.92), distribution coefficients, values for the heat balances in each stage, input substances and initial temperatures are actually obtained by an optimisation process and relate to a particular furnace rather than generically to all Si arc furnaces. The example above is from Eriksson and Hack (1990) but later calculations by the same authors (Eriksson and Hack 1996) give somewhat different results. However, the latter relate to a specific Si arc furnace at KemaNord, Ljungaverk, in Sweden.

10.6.8 Nuclear applications

Nuclear applications constituted a strong area in the early stages of CALPHAD calculations, not only to obtain a better understanding of alloying in U- and Pu-based systems but also for handling complex gas reactions. The interest in applying CALPHAD to nuclear problems is well demonstrated by the papers of Potter and Rand (1980, 1983) which reviewed work on a variety of problems, including simple calculations for the U–O and U–Pt–O systems, and more complex calculations for irradiated fuels and coolant reactions. Recently Ball *et al.* (1989, 1996) have looked at the application of phase-equilibrium calculations to cladding failure in irradiated pins for water-cooled thermal and liquid-metal-cooled fast-breeder reactors and the analysis of accidents in nuclear reactors.

References are listed on pp. 402–408.

10.6.8.1 Cladding failure in oxide fuel pins of nuclear reactors. The long-term operational performance of nuclear fuel pins is critically governed by the reactions that occur in the gap between the fuel and its cladding. Ball *et al.* (1989) examined this for the cases of (1) Zircaloy-clad pellets of UO_{2+x} in a pressurised water reactor (PWR) and (2) stainless-steel-clad pellets of $(U,P)O_{2+x}$ in a liquid-metal-cooled fast-breeder reactor (LMFBR). In particular they were interested in the influence of O potential on Cs, I, Te and Mo and the effects of irradiation on the gaseous species within the fuel-clad gaps.

In the case of PWRs, which operate at relatively low centre temperatures (~1500 K), it was considered that little diffusion of fission product elements would occur to the gap, the majority of material in the gap arising from athermal processes such as fission-fragment recoil. The oxygen potential was taken to increase with increasing irradiation and a series of calculations were made at 650 K to predict the pressure of the predominant gas species as a function of oxygen potential. Two cases were considered: (1), Mo and Zr being zero, i.e., no presence of the fission-product Mo or interaction with the Zircaloy (Fig. 10.93(a)), and (2) with Mo and Zr included (Fig. 10.93(b)). Although qualitatively similar, the calculations show that the inclusion of Mo increased the I pressure in the gas due to the reaction of CsI with Mo-containing species to form Cs_2MoO_4.

In LMBFRs, operating temperatures at the centre are nearer 2300 K, far higher than in PWRs, and the fuel is a mixture of U and P oxide $(U,P)O_{2+x}$. Any reactions must now include Cr from the oxide film of the stainless-steel cladding which has replaced Zircaloy. Figure 10.94(a) then show the calculated ratios of Te:Cs, I:Cs and Te:I for a reaction at 850 K, assuming that no fuel was involved in the reaction, which is then predominantly controlled by Mo and Cr, while Fig. 10.94(b) shows what happens when fuel is included, assuming similar levels of Mo and Cr. Again, the calculations show that predictions are qualitatively similar in both cases, but there are significant differences in the amounts of reaction.

On the basis of the above calculations, Ball *et al.* (1989) concluded that, for PWRs, the potential of I in the gas from equilibrium reactions would be insufficient to account for stress corrosion cracking (SCC) of the Zircaloy. The inclusion of Mo, which can be present in the gap as a fission product, raised the iodine potential but, again, not to a level sufficient to account for any SCC. However, the concentrations of the elemental gaseous species could increase more significantly due to irradiation by fission fragments, and this may be sufficient to produce SCC of the Zircaloy. For the case of LMBFRs, I levels were also increased due to increased O potential. More importantly, Cs and Te levels would also be increased and, with the ratio Te:Cs>0.5, the calculations showed that these elements may deposit as solids onto the cladding surface leading to corrosion of the stainless-steel cladding.

10.6.8.2 Accident analysis during melt-down of a nuclear reactor. The problem to be considered here is the erosion of concrete by liquid material during a 'melt-

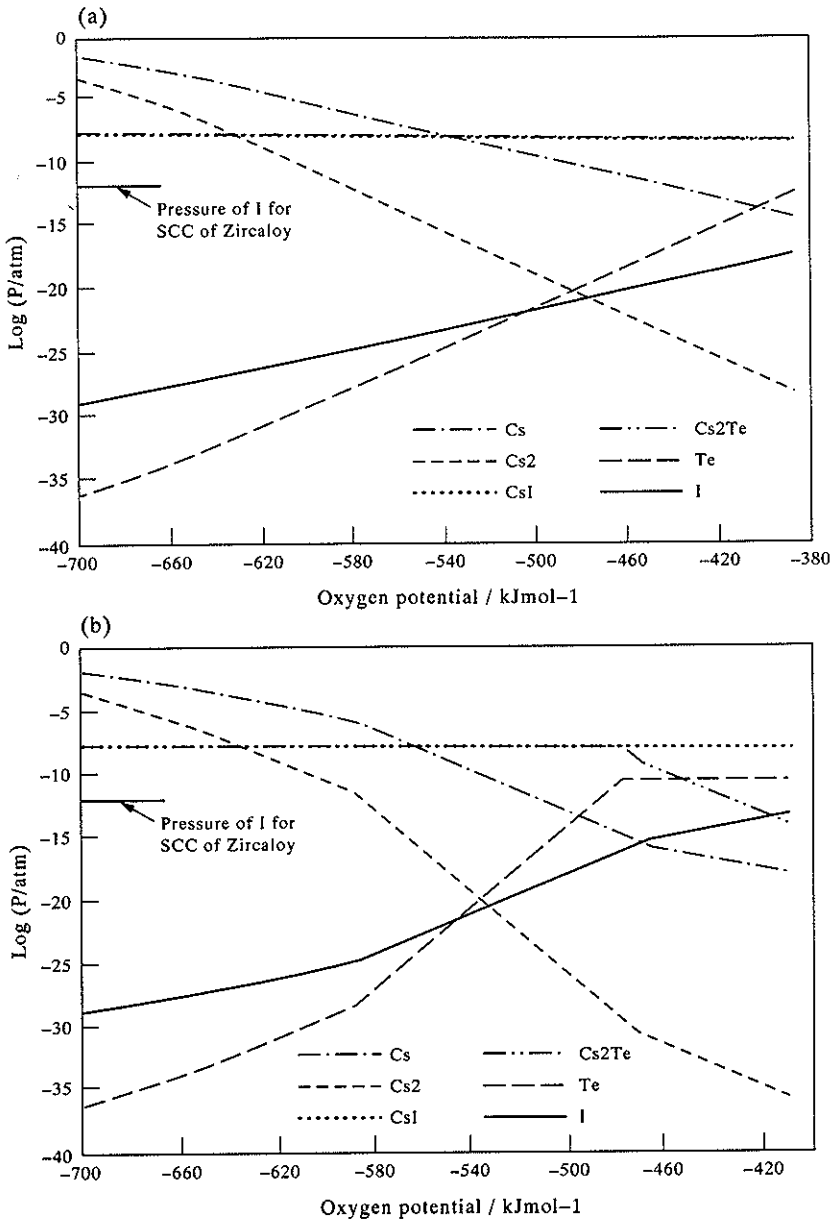

Figure 10.93 Calculated pressures of the predominant gas phase species as a function of oxygen potential within the fuel-clad gap of a PWR fuel pin calculated for the case (a) where Mo and Zr are absent and (b) where Mo and Zr are included (Ball *et al.* 1989).

References are listed on pp. 402–408.

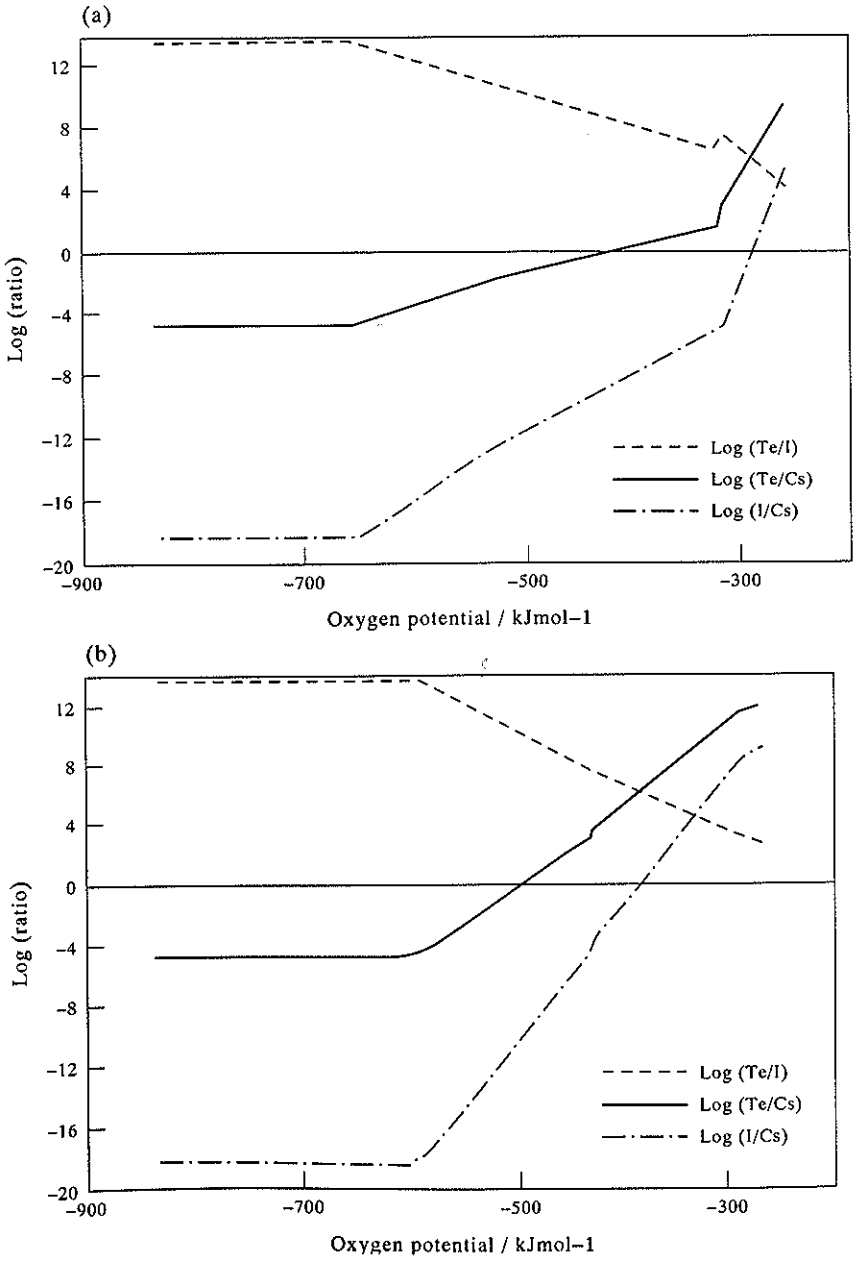

Figure 10.94 Calculated ratios of amounts of Te:Cs, I:Cs and Te:I in the gas phase as a function of oxygen potential within the fuel-clad gap of a LMFBR fuel pin assuming (a) no fuel takes part in the reaction and (b) fuel is included in the reaction (Ball *et al.* 1989).

down' of the reactor core. In this case the liquid core is 'relocated' into the bottom of the reactor vessel where immiscible oxide and metal liquids are formed. This is initially contained within a crucible of condensed material but, if the wall of the reactor pressure vessel is breached, the molten 'corium', comprising components of the core and structural materials, is ejected onto a concrete basemat in the secondary containment building. This concrete basemat is both thermally ablated and attacked by the molten 'corium–concrete' interaction (MCCI). In addition there are gas reactions which can potentially lead to the release of dangerous radioactive material into the atmosphere.

To examine this problem more closely it was necessary to develop (1) a model for the nine-component oxide system UO_2–ZrO_2–SiO_2–CaO–MgO–Al_2O_3–SrO–BaO–La_2O_3 to account for the MCCI (Chevalier 1992, Ball *et al.* 1993) and (2) develop a database for the gas-phase reactions in the oxide subsystem UO_2–ZrO_2–SiO_2–CaO–MgO–Al_2O_3. The final oxide database included four solution phases and 70 condensed stoichiometric phases.

Figures 10.95(a, b) show isopleths calculated between (a) corium and siliceous concrete and (b) corium and limestone concrete. Comparison between experimental (Roche *et al.* 1993) and calculated values for the solidus are in reasonable agreement, but two of the calculated liquidus values are substantially different. However, as the solidus temperature is more critical in the process, the calculations can clearly provide quite good-quality data for use in subsequent process simulations. Solidus values are critical factors in controlling the extent of crust formation between the melt-concrete and melt-atmosphere interface, which can lead to thermal insulation and so produce higher melt temperatures. Also the solidus, and proportions of liquid and solid as a function of temperature, are important input parameters into other software codes which model thermal hydraulic progression and viscosity of the melt (Cole *et al.* 1984).

Calculations including the vapour phase were then made to determine the extent of release of various components during the reaction. Two types of calculation were made, one where ideal mixing in the solution phases was considered and the other where non-ideal interactions were taken into account. For elements such as Ba, U and, to a certain extent, Si, the calculations were relatively insensitive to the model adopted. However, the amount of Sr in the gas was 24 times higher in the 'full model' in comparison to the ideal model. This led to the conclusion that sensitivity analysis was necessary to determine the extent to which accuracy of the thermodynamic parameters used in the model affected the final outcome of the predictions.

10.6.8.3 The effect of radiation on the precipitation of silicides in Ni alloys. While chemical reactions in nuclear generators have dominated how CALPHAD methods have been used in practice for nuclear applications, there has also been a significant interest in the metallurgical aspects of materials under irradiation (Kaufman *et al.*

References are listed on pp. 402–408.

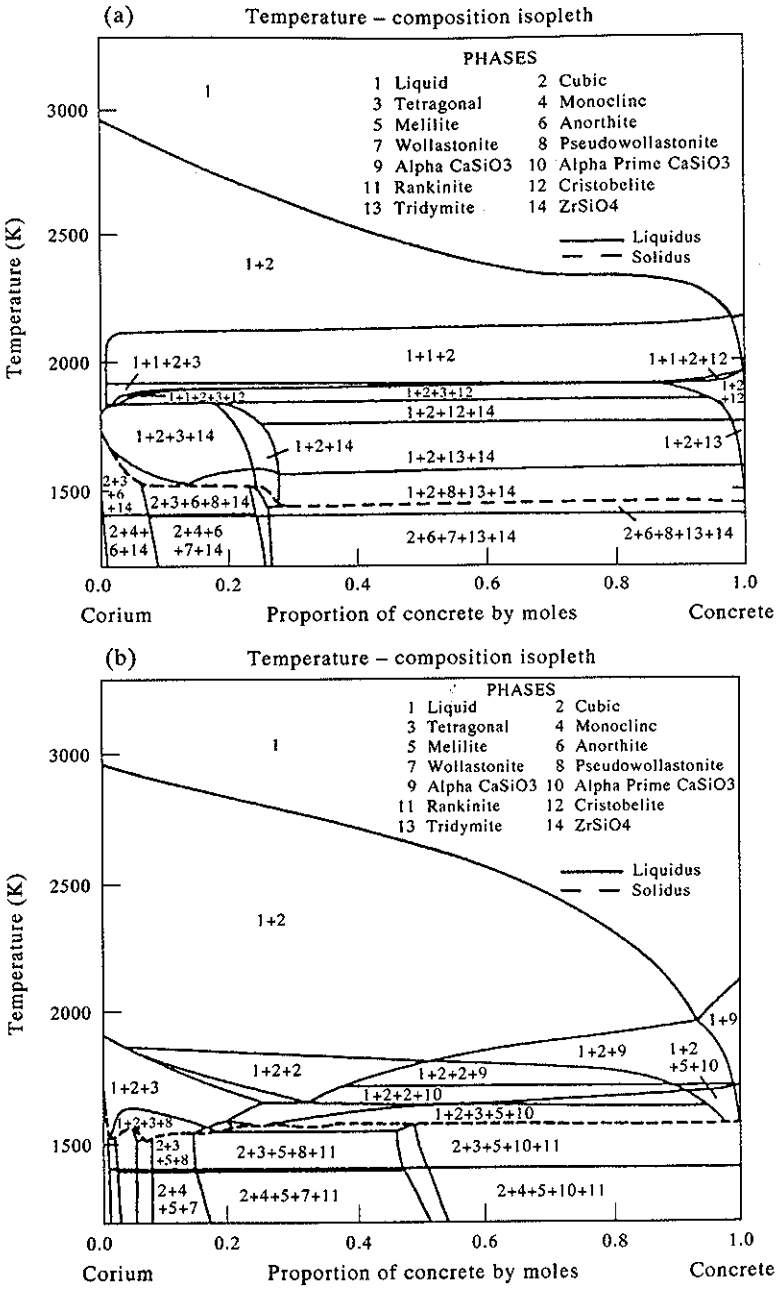

Figure 10.95 Calculated isopleths from 100% corium to 100% concrete. (a) For sicliceous concrete and (b) limestone concrete (Ball *et al.* 1996).

1978, Miodownik *et al.* 1979, Watkin 1979). Irradiation can cause void-swelling, suppression of σ formation in stainless steels and non-equilibrium precipitation of silicides. These phenomena are complex and occur by a combination of thermodynamic and kinetic effects. However, it was shown by Miodownik *et al.* (1979) that a thermodynamic analysis could be used to good effect to rationalise the effect of radiation on silicide formation. Although the work was done for a simple alloy system, it demonstrates how thermodynamics can be used in unusual circumstances.

Barbu and Martin (1977) observed that increasing Ni^+ dose rate enhanced the formation of Ni_3Si in Ni–Si alloys (Fig. 10.96), causing it to form in 'sub-saturated' alloys whose Si levels were below the solvus composition for the formation of equilibrium Ni_3Si. From a purely thermodynamic point of view an additional Gibbs energy (ΔG^*) has to be taken into account which is shown schematically in Fig. 10.97. Miodownik *et al.* (1979) correlated this additional Gibbs energy to dose rate for sub-saturated Ni–Si alloys with 2 and 6at%Si (Fig. 10.98), and generated a diagram which showed how the formation of Ni_3Si would occur in these alloys as a function of temperature and dose rate (Fig. 10.99). The diagram is analogous to a time–temperature–transformation diagram with the dose rate taking the place of the time axis. Rotating the axes also gives a form of diagram similar to that of Barbu and Martin (1977) shown in Fig. 10.96.

Although the work was in the form of pseudo-equilibrium in the presence of irradiation, and did not take into account the effect of kinetics, it nevertheless gives a clear indication of an additional energy term due to irradiation. Similar studies were done by Kaufman *et al.* (1978) to show the magnitude of the Gibbs energy necessary to prevent σ formation in Fe–Cr–Ni alloys.

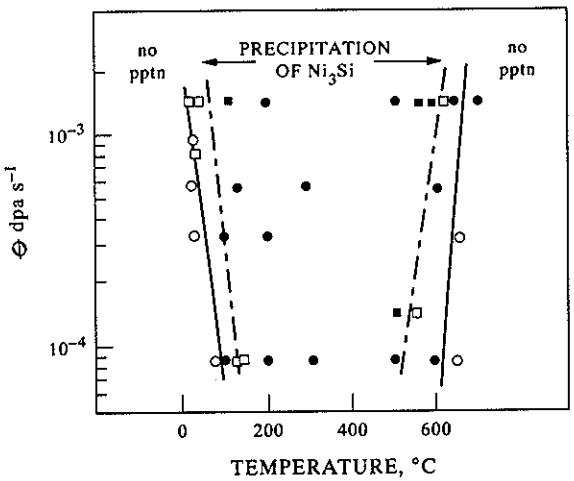

Figure 10.96 Combinations of Ni^+ dose-rate and temperature leading to precipitation of Ni_3Si (from Barbu and Martin 1977).

References are listed on pp. 402–408.

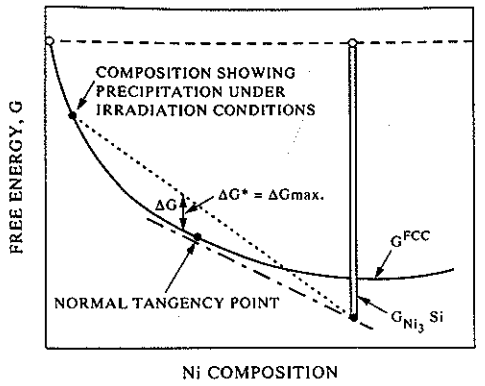

Figure 10.97 Definition of the Gibbs energy (ΔG^*) required in order to precipitate Ni_3Si in subsaturated solid solutions (from Miodownik *et al.* 1979).

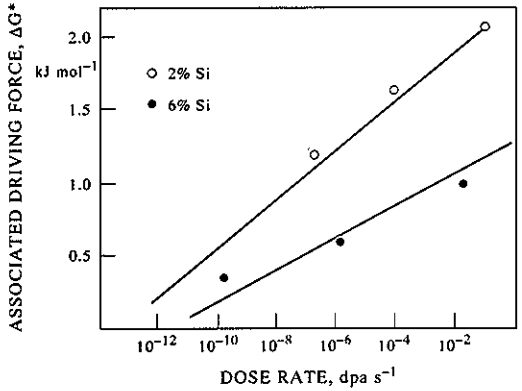

Figure 10.98 Correlation of ΔG^* with dose rate for 2at% and 6at%Si alloys (from Miodownik *et al.* 1979).

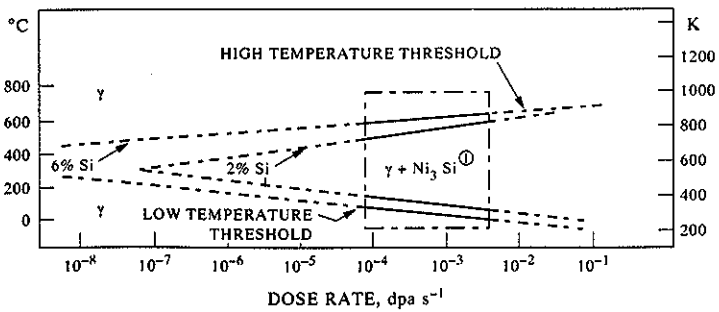

Figure 10.99 Calculated amount of Ni_3Si precipitated in subsaturated Ni–Si alloys in the presence of Ni^+ irradiation (from Miodownik *et al.* 1979).

10.7. SUMMARY

This chapter has shown many examples of the use of CALPHAD methods, ranging from an unusual application in a binary system, through complex equilibrium calculations to calculations for 10-component alloy systems. In all cases the use of CALPHAD methods has enhanced the understanding of processes, clearly defined alloy behaviour and provided vital information for other models, etc. It is also clear that *equilibrium* calculations can be used in many different areas and under a surprising number of different conditions. For numerous reasons, modelling will never completely replace experimental measurement. However, the quantitative verification of the accuracy of CALPHAD calculations now means that they can be seriously considered as an information source which can be used as an alternative to experimental measurement in a number of areas and can also enhance interpretation of experimental results.

For a number of applications, particularly those associated with conditions of continuous cooling or heating, equilibrium is clearly never approached and calculations must be modified to take kinetic factors into account. For example, solidification rarely occurs via equilibrium, amorphous phases are formed by a variety of non-equilibrium processing routes and in solid-state transformations in low-alloy steels much work is done to understand time–temperature–transformation diagrams which are non-equilibrium in nature. The next chapter shows how CALPHAD methods can be extended to such cases.

REFERENCES

Akamatsu, S., Hasebe, M., Senuma, T., Matsumura, Y. and Akisue, O. (1994) *ISIJ International*, **34,** 9.

Andersson, J.-O. (1988) *CALPHAD*, **12,** 1.

Andersson, J.-O. and Sundman, B. (1987) *CALPHAD*, **11,** 83.

Ansara, I. and Rand, M. H. (1980) *The Industrial Use of Thermochemical Data*, ed. Barry, T. I. (Chemical Society, London), p. 149.

Anyalebechi, P. N. (1992) in *Processing, Properties and Application of Metallic and Ceramic Materials*, eds Loretto, M. H. and Beevers, C. J. (MCE publications, UK), p. 219.

Bale, C. W. and Eriksson, G. (1990) *Canadian Metallurgical Quarterly*, **289,** 105.

Ball, R. G. J., Mason, P. K. and Mignanelli, M. A. (1996) in *The SGTE Casebook—Thermodynamics at Work*, ed. Hack, K. (Inst. Materials, London), p. 135.

Ball, R. G. J., Mignanelli, M. A., Barry, T. L. and Gisby, J. A. (1993) *J. Nucl. Materials*, **201,** 238.

Barbu, A. and Martin, G. (1977) *Scripta Met.*, **11,** 771.

Barry, T. I. and Dinsdale, A. T. (1996) in *The SGTE Casebook—Thermodynamics at Work*, ed. Hack, K. (Inst. Materials, London), p. 56.

Betteridge, W. and Heslop, J. (1974) in *The NIMONIC Alloys and other Ni-Based High Temperature Alloys: 2nd Edition*, (Edward Arnold Ltd, 1974).

Bhadeshia, H. K. D. B and Edmond, H. V. (1980) *Acta Met.*, **28,** 1265.

Bhowal, G. E., Konkel, W. A. and Merrick, H. F. (1995) in *Gamma Titanium Aluminides*, eds Kim, Y.-W. *et al.* (TMS, Warrendale, OH), p. 787.

Blavette, B., Caron, P. and Khan, T. (1988) in *Superalloys 1988*, eds Reichman, S. *et al.* (TMS, Warrendale), p. 305.

Blenkinsop, P. (1993) "IRC in materials for high performance applications", University of Birmingham, U.K., private communication.

Boniardi, M., Iacoviello, F. and La Vecchia, G. M. (1994) in *Proc. Conf. Duplex Stainless Steels '94* (Welding Institute, Cambridge), Paper 89.

Brinegar, J. R., Mihalisin, J. R. and Van der Sluis, J. (1984) in *Superalloys 1984*, eds Gell, M. *et al.* (Met. Soc. AIME, Warrendale), p. 53.

Bronson, A. and St-Pierre, G. R. (1981) *Met. Trans. B*, **12B,** 729.

Cama, H., Worth, J., Evans, P. V., Bosland, A. and Brown, J. M. (1997) in *Solidification Processing 1997*, eds Beech, J. and Jones, H. (University of Sheffield, UK), p. 555.

Cao, H.-L. and Hertzmann, S. (1991) in *Proc. Conf. Duplex Stainless Steels '91* (Les Editions Physique, Les Ulis, France), p. 1273.

Caron, P. and Khan, T. (1983) *Mat. Sci. Eng.*, **61,** 173.

Chandrasekaran, L. and Miodownik, A. P. (1989) "Phase equilibria relevant to liquid phase sintering in Fe-base alloys", Report to SERC under contract GR/D 99935 (University of Surrey, Guildford, January).

Chandrasekaran, L. and Miodownik, A. P. (1990) in *PM into the 90s; Proc. Int. Conf. PM90* (Inst. Metals, London), p. 398.

Charles, J., Dupoiron, F., Soulignac, P. and Gagnepain, J. C. (1991) in *Proc. Conf. Duplex Stainless Steels '91* (Les Editions Physique, Les Ulis, France), p. 1273.

Chart, T. G., Putland, F. and Dinsdale, A. T. (1980) *CALPHAD*, **4,** 27.

Chatfield, C. and Hillert, M. (1977) *CALPHAD*, **1,** 201.

Chen, C. C. and Sparks, R. B. (1980) in *Titanium Science and Technology*, eds Kimura, H. and Izumi, O. (Met. Soc. AIME, Warrendale), p. 2929.

Chevalier, P. Y. (1992) *J. Nucl. Materials*, **186,** 212.

Cole, R. K., Kelley, D. P. and Ellis, M. A. (1984) "CORCON-Mod 2: A computer programme for analysis of molten core–concrete interactions", NUREG/CR-3920, August.

Counsell, J. F., Lees, E. B and Spencer, P. J. (1972) in *Metallurgical Thermochemistry* (NPL–HMSO, London), p. 451.

Cortie, P. and Potgeiter, J. H. (1991) *Met. Trans. A*, **22A,** 2173.

Darolia, R., Lahrman, D. F. and Field, R. D. (1988) in *Superalloys 1988*, eds Reichmann, S. *et al.* (TMS, Warrendale), p. 255.

Delargy, K. M. and Smith, G. D. W. (1983) *Met. Trans. A*, **14A,** 1771.

Dharwadkar, S. R., Hilpert, K., Schubert, F. and Venugopal, V. (1992) *Z. Metallkde.*, **83,** 744.

Dinsdale, A. T. (1991) *CALPHAD*, **15,** 319.

Dinsdale, A. T., Hodson, S. M., Barry, T. I. and Taylor, J. R. (1988) *Computer Software in Chemical & Extractive Metallurgy*, Proc. Met. Soc. CIM, Montreal '88, **11.**

Dreshfield, R. L. and Wallace, J. F. (1974) *Met. Trans*, **5,** 71.

Duerig, T. W., Terlinde, G. T. and Williams, J. C. (1980) *Met. Trans. A*, **11A,** 1987.

Duval, S., Chambreland, S., Caron, P. and Blavette, D. (1994) *Acta Met. Mat.*, **42,** 185.